
Examples of EO-1 Hyperion Data Analysis

Michael K. Griffin, Su May Hsu, Hsiao-hua K. Burke,
Seth M. Orloff, and Carolyn A. Upham

■ The Earth Observing 1 (EO-1) satellite has three imaging sensors: the multispectral Advanced Land Imager (ALI), the hyperspectral Hyperion sensor, and the Atmospheric Corrector. Hyperion is a high-resolution hyperspectral imager capable of resolving 220 spectral bands (from 0.4 to 2.5 micron) with a 30 m resolution. The instrument images a 7.5 km by 100 km surface area. Since the launch of EO-1 in late 2000, Hyperion is the only source of spaceborne hyperspectral imaging data. To demonstrate the utility of the EO-1 sensor data, this article gives three examples of EO-1 data applications. A cloud-cover detection algorithm, developed for processing the Hyperion hyperspectral data, uses six bands in the reflected solar spectral regions to discriminate clouds from other bright surface features such as snow, ice, and desert sand. The detection technique was developed by using twenty Hyperion test scenes with varying cloud amounts, cloud types, underlying surface characteristics, and seasonal conditions. When compared to subjective estimates, the algorithm was typically within a few percent of the estimated total cloud cover. The unique feature-extraction capability of hyperspectral sensing is also well suited to coastal characterization, which is a more complex task than deep ocean characterization. To demonstrate the potential value of Hyperion data (and hyperspectral imaging in general) to coastal characterization, EO-1 data from Chesapeake Bay are analyzed. The results compare favorably with data from other satellite and aircraft data sources. Finally, to demonstrate additional utility of EO-1 data, we describe how a combined analysis of panchromatic, multispectral, and hyperspectral data can be applied to terrain characterization and anomaly detection.

HYPERSPECTRAL IMAGING SENSORS have been used for more than a decade to aid in the detection and identification of diverse surface targets, topographical details, and geological features. Techniques for scene characterization can utilize individual or combined spectral bands to identify specific features in an image. This article describes three examples of surface characterization, using data from the hyperspectral Hyperion sensor and the multispectral Advanced Land Imager (ALI) sensor on the Earth Observing 1 (EO-1) satellite.

The first example deals primarily with the problem of discrimination of clouds from surface features. A simplified cloud detection algorithm was developed that utilizes only reflected solar measurements from the EO-1 Hyperion sensor to discriminate clouds from all other features in the image [1]. This cloud detection effort was part of the EO-1 Extended Mission Phase of the EO-1 Science Program. The overall effort was designed to demonstrate the potential for performing cloud-cover detection onboard the satellite to regulate which scenes would be transmitted

for ground processing. The effort involved retrieving a collected Hyperion image into onboard memory, calibrating the image data to radiance, converting the radiances to at-sensor or top-of-the-atmosphere reflectances, and performing the cloud-cover detection. The last two steps of this process—conversions of radiance to reflectance and cloud-cover detection—are described in this article. This work represents the first time that an application such as cloud detection was performed onboard a spaceborne sensor.

The second example demonstrates the potential value of Hyperion data (and hyperspectral imaging in general) to perform coastal characterization. Oceans comprise two-thirds of the earth surface. Remote sensing provides the only reasonable way of monitoring and understanding this enormous part of our planet. Optical properties of natural bodies of ocean water are influenced by many factors. Some of the key substances affecting ocean characteristics are phytoplankton, suspended material, and organic substances. Spectral remote sensing provides a means of routinely obtaining information on ocean properties [2–4]. EO-1 data collected over Chesapeake Bay from 19 February 2002 are analyzed. Hyperion data are first compared with multispectral ALI data to gain insights into what additional information content hyperspectral data can provide. A simple algorithm for chlorophyll retrieval is also applied. The results compare favorably with data from other sources.

In the third example, a combined analysis of panchromatic, multispectral, and hyperspectral data is shown to demonstrate additional utility of EO-1 data for terrain characterization, anomaly detection, feature extraction, and spectral unmixing. Data sets from the Coleambally Irrigation Area, Australia, on 7 March 2000 and the San Francisco Bay area on 17 January 2000 are employed for the analysis. Various tools for terrain analysis to delineate and characterize vegetation and soil are applied. These soil and vegetation fields are further clustered according to variations in their spectral characteristics.

EO-1 Sensors

The NASA New Millennium Program's EO-1 satellite was successfully launched on 21 November 2000. There are three primary instruments on the EO-1 spacecraft: the multispectral Advanced Land Imager (ALI), the hyperspectral Hyperion sensor, and the Linear Etalon Imaging Spectrometer Array (LEISA) Atmospheric Corrector (LAC). The EO-1 platform was positioned on orbit to be approximately one minute behind the Landsat 7 Enhanced Thematic Mapper Plus (ETM+) sensor at an altitude of 705 km [5]. With the demise of the Lewis and Orbview-4 spacecrafts, EO-1 uniquely offers a spaceborne spectral imaging capability that is not currently available from any other source [6]. Table 1 summarizes the essential spatial and spectral characteristics of Landsat 7

Table 1. Landsat and EO-1 Instrument Overview

Parameters	Landsat 7 ETM+	EO-1 ALI	EO-1 Hyperion	EO-1 LAC
Spectral range	0.4–2.4 μm *	0.4–2.4 μm	0.4–2.5 μm	0.9–1.6 μm
Spatial resolution	30 m	30 m	30 m	250 m
Swath width	185 km	37 km	7.5 km	185 km
Spectral resolution	variable	variable	10 nm	3–9 nm**
Spectral coverage	discrete	discrete	continuous	continuous
Panchromatic-band resolution	15 m	10 m	N/A	N/A
Number of bands	7	10	220	256

* Excludes thermal channel

** 35/55 cm^{-1} constant resolution

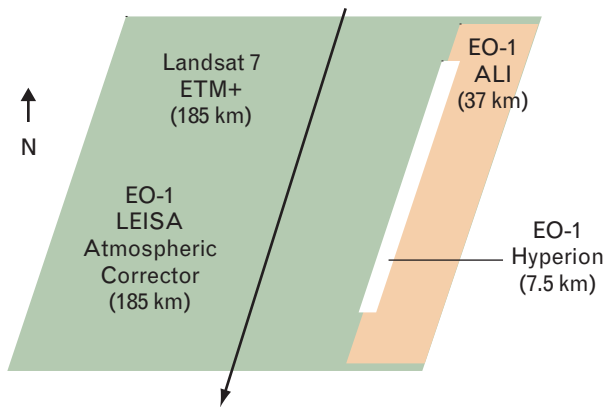


FIGURE 1. Instrument ground tracks for the Landsat 7 Enhanced Thematic Mapper Plus (ETM+) sensor and the three EO-1 sensors: the Advanced Land Imager (ALI), Hyperion, and the Linear Etalon Imaging Spectrometer Array (LEISA) Atmospheric Corrector (LAC). Hyperion is a push-broom imaging sensor with a swath width of 7.5 km. The EO-1 platform was positioned on orbit to be approximately one minute behind the Landsat 7 ETM+ sensor at an altitude of 705 km.

and the EO-1 instrument suite. Figure 1 illustrates the overlap in surface area coverage of the ALI, Hyperion, and LAC sensors, compared to the Landsat 7 ETM+ ground track [7].

ALI employs a 15° wide-field telescope and a partially populated focal plane occupying one fifth of the field of view, giving a ground swath width of 37 km. The ALI was designed to be a follow-on type of sensor with bands and spatial resolution similar to the Landsat 7 sensor. Hyperion is a grating imaging spectrometer providing 10 nm (sampling interval) contiguous bands in the solar reflected spectrum from 0.4 to 2.5 μm with a spatial resolution of 30 m (the same as the ALI and Landsat sensors) over a 7.5 km swath. Each swath, or line of data, contains 256 pixels. LAC is an imaging spectrometer covering the spectral range from 0.9 to 1.6 μm , but with a spatial coverage in the hundreds of meters to monitor the atmospheric water absorption lines for correction of atmospheric effects in multispectral imagers.

Hyperion Cloud-Cover Analysis

This section deals primarily with the problem of discrimination of clouds from surface features. Most cloud detection or cloud-mask schemes utilize both solar reflected (visible, near infrared, and shortwave

infrared) and thermal emitted (midwave and long-wave infrared) measurements [8]. Longwave infrared (LWIR) data provide information on the physical temperature of the cloud and the surface, which can be a useful discrimination tool. Reflected solar measurements, common to many hyperspectral imaging sensors, rely primarily on spectral reflectance differences to discriminate scene features. A simplified cloud detection algorithm has been developed that utilizes only reflected solar measurements from the EO-1 Hyperion sensor to discriminate clouds from all other features in the image [1].

Algorithm Description

The Hyperion cloud-cover algorithm utilizes only six Hyperion bands to discriminate all types of clouds from other surface features in a scene. The selection of the six bands provided spectral information at critical wavelengths while keeping computer processing costs to a minimum. This trade-off was a key aspect of the entire cloud-cover detection process, since both onboard computer memory and processing time were limited. Table 2 lists the six bands chosen for the initial form of the cloud-cover algorithm. They include two visible channels, a near-infrared channel and three shortwave infrared (SWIR) channels.

Table 2. Hyperion Bands Used in the Cloud-Cover Algorithm

Band (μm)	Usage
0.55	Snow/ice/cloud test
0.66	Red reflectance test Vegetation ratio test
0.86	Vegetation ratio test
1.25	Snow/ice/cloud test Desert and sand test
1.38	High cloud test Ice and low cloud test
1.65	Snow/ice/cloud test Desert and sand test

Hyperion has two detectors, the first covering the visible and near infrared while the second covers the SWIR bands. The current algorithm requires channels from both detectors. An algorithm using only visible and near-infrared bands was considered in order to reduce processing time, but cloud-cover detection results were not good for scenes with bright surfaces such as desert, snow, or ice. In utilizing these six channels, formulas relating the spectral measurements were adapted or developed to discriminate and identify cloud features in a scene. Figure 2 provides a flowchart of the Hyperion cloud-cover algorithm. A brief description of the phenomenology behind the algorithm follows. Each test detailed below is designed to eliminate specific non-cloud features while allowing potential cloud pixels to pass on to the next test.

Conversion of Radiance to Reflectance

Channels with center wavelengths up to 3 μm derive their signal from reflected solar energy off land, water,

and cloud features. The amount of solar energy that is reflected provides information about surface and atmospheric feature characteristics such as absorption and scattering properties. The reflectivity of an object in a scene is generally not a function of the incident solar insolation (although it is a function of the viewing geometry). Therefore, deriving the apparent or at-sensor reflectivity for a scene can remove the variation in the solar illumination with wavelength.

For the Hyperion sensor, where reflected solar flux is the primary illumination source, it is useful to convert the channel radiance L_i to an *at-sensor* reflectance ρ_i , where the subscript i denotes a Hyperion band. This conversion can be accomplished by dividing the channel radiance by the incident solar flux $F_{0,i}$ corrected for sun angle μ_0 and earth-sun distance $d_{\text{earth-sun}}$ in astronomical units (AU):

$$\rho_i = \left(\frac{\pi}{\mu_0 F_{0,i} / d_{\text{earth-sun}}^2} \right) L_i . \quad (1)$$

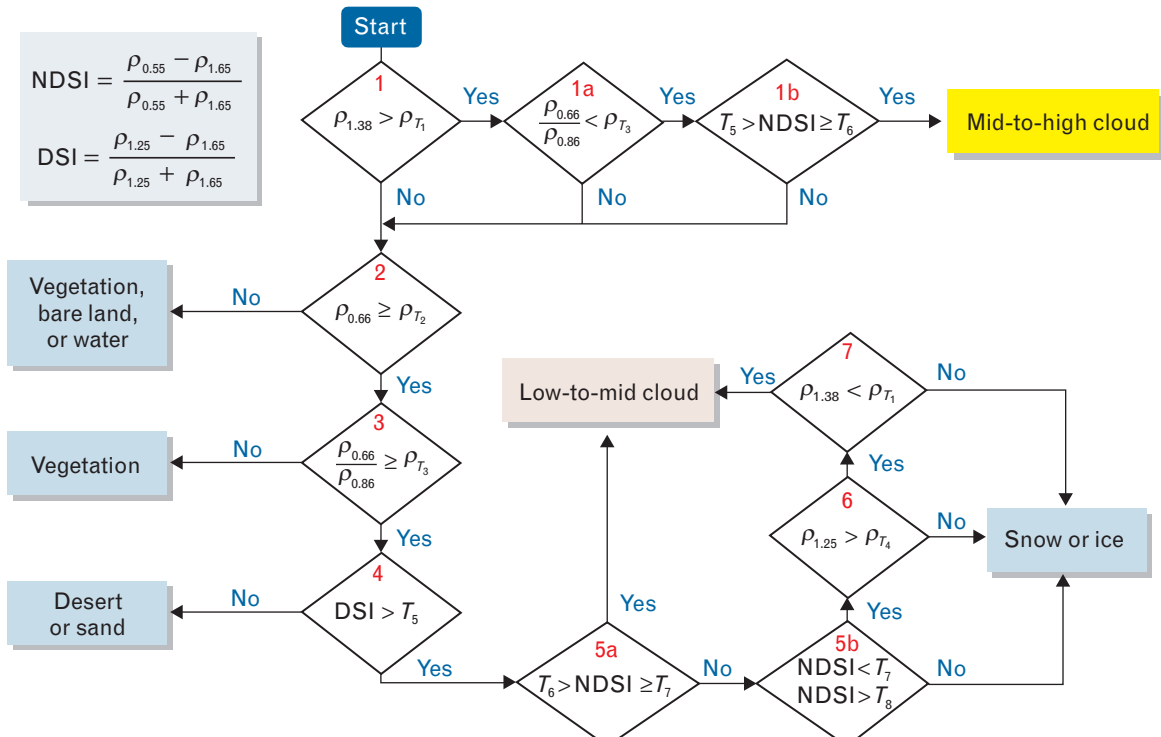


FIGURE 2. Flowchart of the detection process in the Hyperion cloud-cover algorithm. The normalized difference snow index (NDSI) and the desert sand index (DSI) are two of the tests used by the algorithm to classify image pixels. The various ρ values represent the computed reflectance for the different spectral bands. The subscripted values of T represent thresholds of the DSI and the NDSI in the detection process.

The sun angle is defined by $\mu_0 = \cos(\theta_0)$, where θ_0 is the solar zenith angle. The solar zenith angle may be obtained through the EO-1 telemetry or it can be calculated from the measurement date, time of day, and geographical location. The earth-sun distance measure $d_{\text{earth-sun}}$ adjusts the mean solar flux $F_{0,i}$ for orbital radius changes. The earth-sun distance is a function of the Julian day and is computed by using a parameterized function of tabulated earth-sun distance variations.

The incident solar flux as a function of wavelength $F_0(\lambda)$ can be obtained from a number of sources; the MODTRAN radiative transfer model [9] contains a solar illumination database that can be easily adapted to the computation in the above equation. The solar flux must be convolved with the Hyperion-band spectral response functions to obtain the channel solar flux $F_{0,i}$. Equation 1 is then applied to each band radiance image to obtain an equivalent set of reflectance images.

Hyperion measurements are distributed as scaled radiance. True radiance is obtained by dividing the scaled radiance by a factor (either 40 or 80) based upon the channel number. Hyperion radiances are archived in units of $\text{W/m}^2\text{-sr}\cdot\mu\text{m}$. The popular unit of radiance for hyperspectral and other applications is the μflick ($\mu\text{W/cm}^2\text{-sr}\cdot\mu\text{m}$), which can be obtained by multiplying the Hyperion radiance values by 100.

High Clouds

High clouds typically have spectral reflectance characteristics that are similar to other cloud types. However, high thin clouds that are predominantly ice are generally not opaque to underlying surface reflectance, such that surface features can be observed through the clouds. This adds a level of difficulty in detecting high clouds, especially if LWIR information is not available. Techniques using observations in the strong water vapor absorption bands have provided a new method to discriminate high clouds from low clouds and surface features [10, 11]. At these wavelengths the water vapor absorption is typically strong enough to completely suppress the contribution from both the reflectance from the surface and low-altitude clouds while adequately transmitting radiation scattered from high-altitude clouds. This allows the possibility for discriminating high clouds from lower-altitude clouds

and surface features by using only a simple reflectance threshold test.

However, in polar latitudes or at high surface elevations, the amount of moisture in the atmosphere is greatly reduced, resulting in reduced water vapor absorption in the $1.38\ \mu\text{m}$ band. This increases the penetration of observations at these wavelengths and increases the possibility of a significant surface reflectance contribution to the signal. For these cases, bright surface features (snow or ice) may be mistaken for high clouds and further testing is required to discriminate these features. A band ratio test is applied to eliminate ice surfaces, and the normalized difference snow index (NDSI) is used to eliminate snow features. Both tests are also used later on in the processing and are described in more detail below. All pixels that are not flagged as high cloud are passed on for further testing.

Reflectance at $0.66\ \mu\text{m}$

Clouds are typically one of the brightest features in a Hyperion image. The reflectance from clouds is nearly invariant in the visible and near-infrared window regions, since the size of the scatterers in the cloud are much larger (i.e., size parameter is much greater than 1) than the sensor wavelengths. This information can be used to discriminate clouds from darker background objects and from bright but spectrally variable surface features.

In the visible spectral band, dark surface objects can be distinguished from bright clouds by a simple reflectance threshold test. At $0.66\ \mu\text{m}$, many surface features such as water, vegetation, shadowed areas, and soil exhibit low reflectance values (less than 0.15) and can be easily flagged. Pixels that fail this threshold test are flagged clear; all other pixels are passed on for further testing. Errors with this test can occur for low sun conditions, which can reduce the cloud reflectance, or for some types of clouds (i.e., cumulus), which can self-shadow.

Vegetation Index Ratio

Vegetated surfaces exhibit a strong reflectance gradient near $0.7\ \mu\text{m}$, known as the *red edge* [12]. The reflectance for vegetation changes from approximately 0.1 in the visible to 0.4 or greater in the near infrared, depending on specific aspects of the vegetation

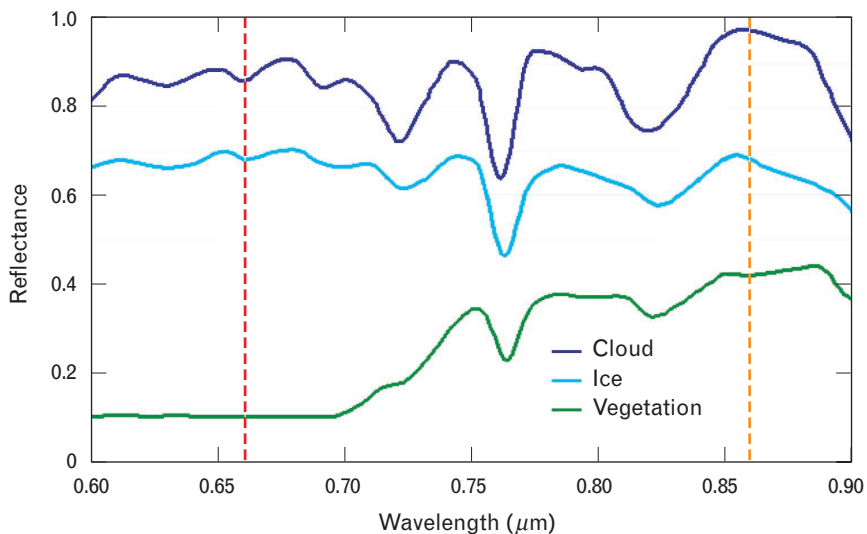


FIGURE 3. Spectral signatures of three features in the visible and near infrared: clouds, surface ice, and vegetation. The red and orange vertical lines represent locations of the visible ($0.66\text{ }\mu\text{m}$) and near-infrared ($0.86\text{ }\mu\text{m}$) bands, respectively, used in the vegetation index ratio test.

cover (such as health and greenness). Clouds, however, display a nearly constant reflectance signal over this range. Therefore, a ratio of a visible to a near-infrared channel should be close to 1.0 for clouds and less than 0.5 for vegetated surfaces. In general, clouds have slightly less reflectance in the visible than in the near infrared. Snow and ice surfaces have a similar behavior to clouds in this spectral region. Figure 3 shows an example of Hyperion-observed spectral reflectance values for clouds, surface ice, and vegetation.

Desert Sand Index

Bright surface features such as snow, ice, and sand can easily be mistaken for cloud features in the visible portion of the spectrum. It is important to be able to distinguish these bright surface features from similarly bright clouds. Desert sand is composed of numerous minerals, including quartz, that strongly reflect sunlight. In contrast to other bright surface features such as snow and ice, desert sand tends to display the largest reflectance near $1.6\text{ }\mu\text{m}$, whereas snow and ice show peaks in the visible and near infrared. Clouds also tend to display higher reflectance values in the infrared with a noticeable drop in reflectance in the SWIR.

These observations provide an empirical means to formulate a discrimination index, or desert sand index

(DSI), similar to vegetation indices. The DSI was derived to highlight the change from low to high reflectance in the visible and near-infrared spectral region for desert and sand surface types. It uses the change in reflectance from the edge of the near infrared to the SWIR, as shown in the formula below:

$$\text{DSI} = \frac{\rho_{1.25} - \rho_{1.65}}{\rho_{1.25} + \rho_{1.65}}.$$

Figure 4 shows plots of the Hyperion-observed spectral reflectance values for snow, ice, desert, and cloud features. Comparing values near the red ($1.25\text{ }\mu\text{m}$) and orange ($1.65\text{ }\mu\text{m}$) vertical bands shows that the sand feature is the only one that displays a negative DSI value. This test provides a process for eliminating bright sand and desert surfaces from consideration as cloud.

Normalized Difference Snow Index

The NDSI is used to identify snow-covered and ice-covered surfaces and to separate snow and ice from cumulus clouds. The NDSI measures the relative difference between the spectral reflectance in the visible and SWIR. The technique is analogous to the normalized difference vegetation index (NDVI), which provides a measure of the health and greenness of vegetated sur-

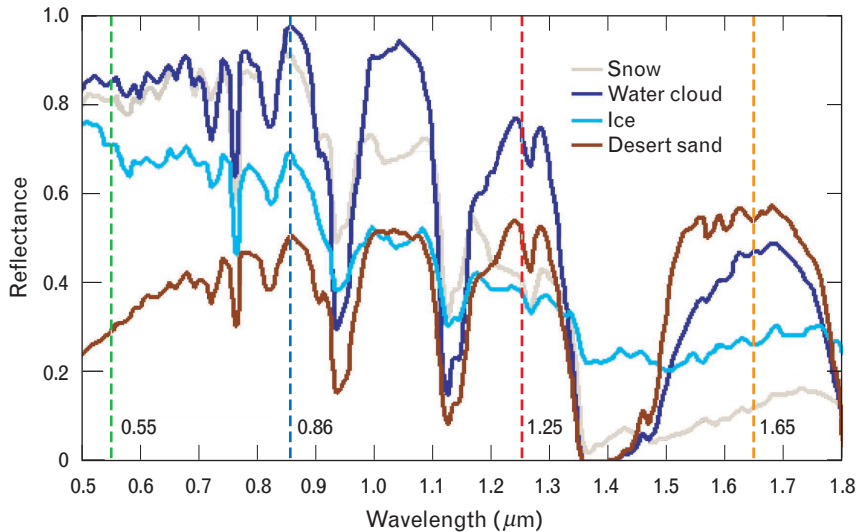


FIGURE 4. Spectral signatures for four features in the visible, near infrared, and shortwave infrared (SWIR): clouds, surface ice, snow, and desert sand. The red and orange vertical bands represent locations of the near-infrared and SWIR channels, respectively, used in the desert sand index test. The green and blue bands represent channels used in the snow and ice discrimination tests.

faces [12]. The formula commonly used for the NDSI is given by

$$\text{NDSI} = \frac{\rho_{0.55} - \rho_{1.65}}{\rho_{0.55} + \rho_{1.65}}.$$

NDSI values greater than approximately 0.4 are representative of various snow-covered conditions with pure new snow having the highest NDSI values. The NDSI tends to decrease as other features (such as soil and vegetation) are mixed in with the snow.

Reflectance at 1.25 μm

Some moderately bright surface features (such as aged or shadowed snow) may fail the NDSI test. Many of these features can be eliminated from consideration as clouds by comparing their reflectance at 1.25 μm to an empirically defined threshold. Most surface features have reflectance values less than 0.4 at this wavelength, while clouds still display reflectances greater than 0.4 (as seen in Figure 4). The 1.25 μm reflectance test is applied only to potential cloudy pixels that have survived previous tests.

Ice Discrimination

To further discriminate ice surfaces from water cloud pixels, pixels that have passed previous tests and have

reflectance values greater than 0.1 at 1.38 μm are assumed to be ice surfaces and eliminated from consideration as cloudy. Again, Figure 4 shows that for water clouds and bright snow-covered surfaces, reflectance values at 1.38 μm are quite low, much less than 0.1. Ice surfaces, however, display a significant reflectance signal at this wavelength. Since ice cover tends to occur during winter months when the air is normally quite dry, this surface feature can often be seen in the 1.38 μm water vapor band and can be mistaken for mid-to-high level clouds.

Algorithm Applications

The cloud-cover detection process defined in Figure 2 was applied to a set of twenty Hyperion scenes with varying cloud cover, cloud type, surface characteristics, and seasonal collection times. Each scene was converted from radiance to reflectance by using the technique described earlier. The cloud-cover detection algorithm was applied independently to each pixel in a scene; effects from adjacent pixels did not influence the computation. While the tests we have just described can discriminate specific surface features from clouds, no attempt was made at this time to classify the surface features on the basis of the results from the tests. A simple cloud/no-cloud mask was provided as the pri-

mary output product, along with line-by-line statistics of the presence of cloud-free pixels, low-to-mid-level cloud (presumably water), and mid-to-high-level cloud (presumably ice). Figures 5 through 10 show examples of the Hyperion scenes used in the evaluation of the algorithm. A red-green-blue (RGB) rendition of the test scene is shown along with the computed cloud mask for each scene. While full Hyperion scenes normally comprise over 3000 lines, only 1000-line subsets of each scene are shown for display purposes. The figure caption gives the computed cloud amount for

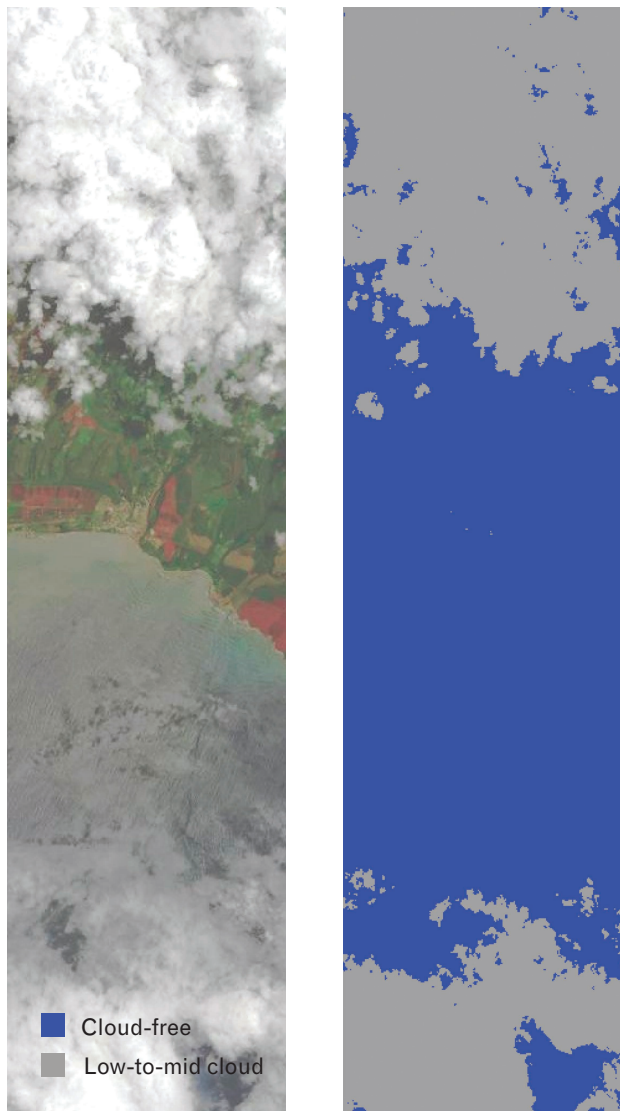


FIGURE 5. Hyperion image collected over Kauai, Hawaii, displaying partly cloudy conditions with cumulus clouds over land and water. The algorithm computed the cloud amount for the scene to be 41.3%.

the 1000-line scene subset. For each of the test scenes, the associated figure depicting the cloud cover uses the following color scheme: blue represents cloud-free, gray or maroon represents low-to-mid cloud, and orange represents mid-to-high cloud.

Kauai, Hawaii

The scene in Figure 5 was collected on 22 May 2002 at 2056 UTC over the island of Kauai, Hawaii. This scene is characterized by partly cloudy conditions with cumulus clouds present over land and water. Clear re-



FIGURE 6. Hyperion image collected near Cheyenne, Wyoming, displaying partly cloudy conditions with high thin clouds over snow-covered hilly terrain. The algorithm computed the cloud amount for the scene to be 58.9%.

gions are also visible. The algorithm does well detecting clouds over land; over the water the main cloud region is masked but some areas of thin cloud cover may not be identified. The $0.66 \mu\text{m}$ threshold reflectance test is the predominant test used over the water for non-ice clouds. Adjusting the threshold value would allow the capture of more clouds over the water. Over the land area, both the reflectance and ratio tests are primarily used to discriminate the clouds from underlying vegetation. The routine seems to miss a small amount of cloud cover over land, mostly cloud edges, which would support a slight reduction in the threshold value for the reflectance test. The total computed cloud amount for this scene segment is 41.3%, which appears to underestimate the actual cloud cover by at most a few percent.

Cheyenne, Wyoming

The scene in Figure 6 was collected on 5 March 2002 at 1720 UTC near Cheyenne, Wyoming. This scene is characterized by partly cloudy conditions with high thin clouds overlying snow-covered hilly terrain. The visible clouds are identified as mid-to-high level clouds by the $1.38 \mu\text{m}$ threshold reflectance test. The clouds are thin enough that some of the underlying terrain is visible, especially near the bottom of the scene. The NDSI test accurately identifies the bright snow-covered terrain as a surface feature, with the possible exception of some areas near the edge of the high clouds. Here the snow-covered surface is masked as a low-to-mid cloud. These areas seem to be either shadowed by the high clouds or self-shadowed due to terrain variations and the moderate sun elevation (36° above the horizon). The regions of possible misidentification comprise only a small percentage of the image (< 4%). The overall computed cloud amount for the scene is 58.9%, which appears to be an overestimate in this case.

Kansas City, Kansas

The scene in Figure 7 was collected near Kansas City, Kansas, on 4 March 2002 at 1638 UTC. This image is characterized by thin mid-level clouds overlying snow-covered terrain. Some river and road features are observable. The algorithm correctly identifies all of the thin cloud cover, but also misidentifies apparently

clear areas as cloud. These areas are located in the upper right quadrant of the image. As with the Cheyenne, Wyoming scene, these seem to be areas of darker snow-covered terrain. The algorithm fails to identify these regions as snow since the NDSI values fall below the nominal threshold for snow. Further tests do not eliminate these features and they are identified as low-to-mid cloud. For this case the amount of clear land misidentified as cloud is approximately 3 to 7%. The overall computed cloud cover for this scene is 72.6% and appears to be an overestimate by about 5%.

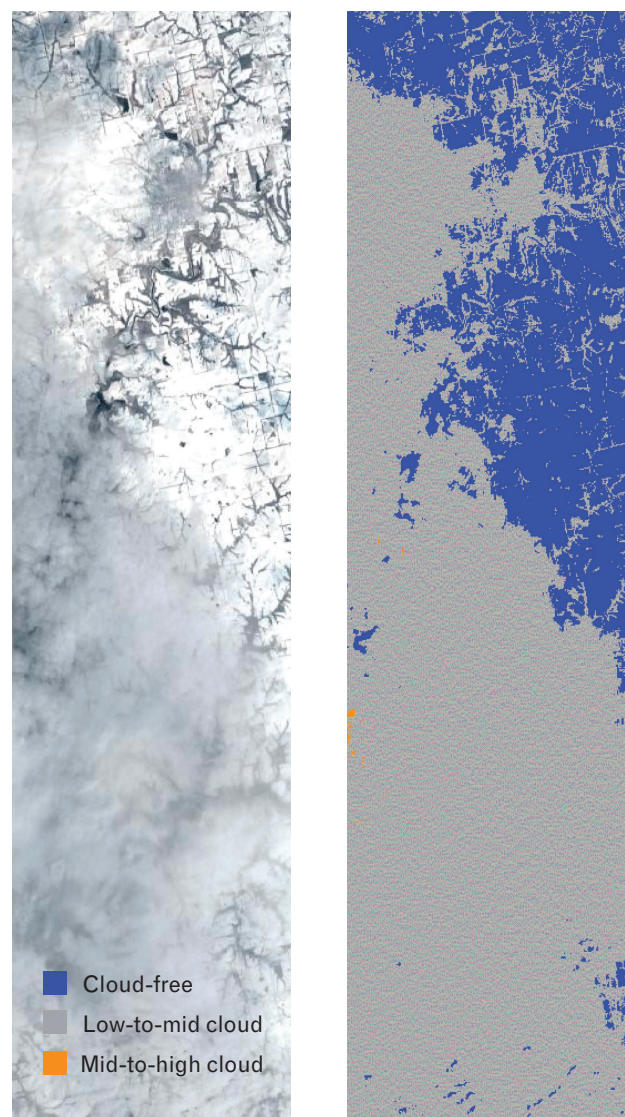


FIGURE 7. Hyperion image collected near Kansas City, Kansas, displaying partly cloudy conditions with thin mid-level clouds over snow-covered terrain. The algorithm computed the cloud amount for the scene to be 72.6%.

Chiefs Island, South Africa

The scene in Figure 8 was collected on 16 April 2002 at 0821 UTC near Chiefs Island, South Africa. Various types of cumulus clouds are present. The algorithm does an adequate job of identifying the majority of the cloud fields, although some of the cloud street patterns near the center of the image are missing from the cloud mask. The $0.66 \mu\text{m}$ reflectance test is predominantly used to identify these types of clouds, and a lowering of the threshold might improve the cloud-

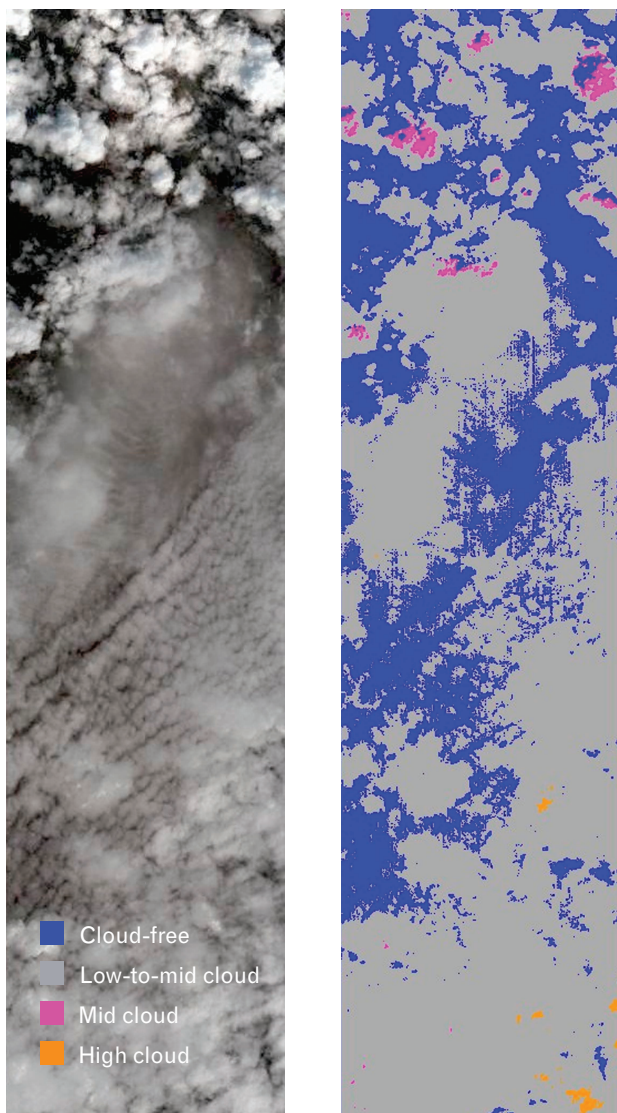


FIGURE 8. Hyperion image collected near Chiefs Island, South Africa, displaying mostly cloudy conditions with a variety of cumulus cloud fields present. The algorithm computed the cloud amount for the scene to be 68.9%.

cover detection. The overall computed cloud amount for this image is 68.9%, which seems to be an underestimate by about 5 to 10%.

Bering Sea

The scene in Figure 9 was collected in the Bering Sea on 20 April 2002 at 2318 UTC. This scene is one of a number of clear scenes over bright surfaces that were chosen to test the ability of the algorithm to discriminate bright surface features from clouds. In this case, the scene is predominantly snow-covered ice and land

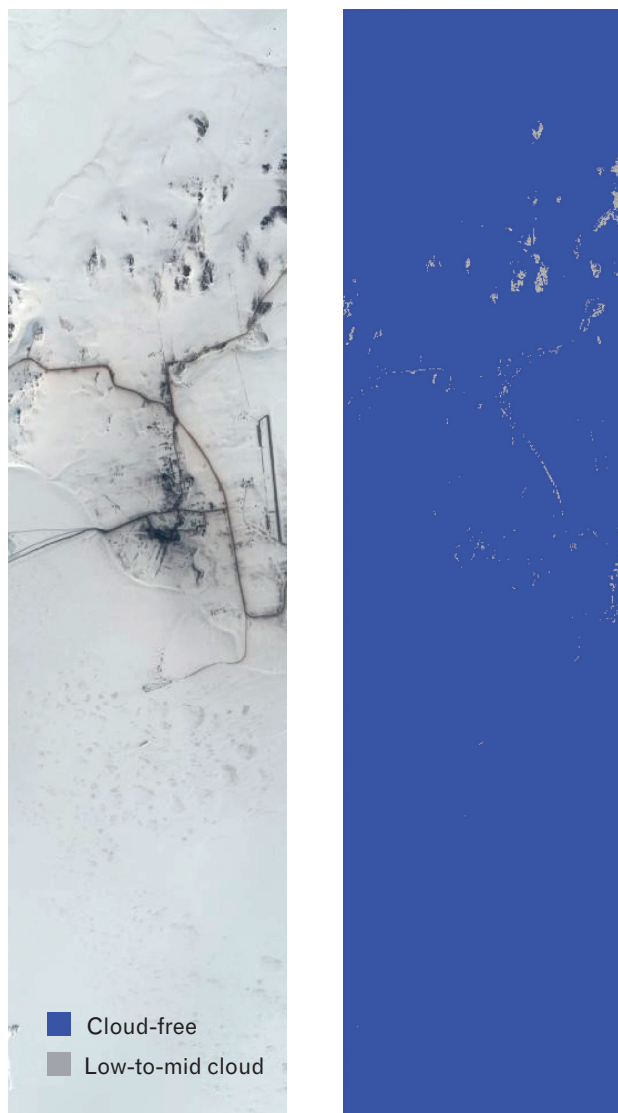


FIGURE 9. Hyperion image collected in the Bering Sea, displaying clear conditions over both snow-covered ice and land. The algorithm computed the cloud amount for the scene to be 0.7%.

with a coastline feature running horizontally across the center of the image and with ice towards the bottom of the image. Some road and man-made structure features are apparent near the center of the image. The algorithm does an excellent job identifying the snow and ice features as cloud free. A small amount of the dark features in the upper part of the image were misclassified as cloud; the computed cloud amount for this image was 0.7%.

Suez Canal

The scene in Figure 10 was collected over the Suez Canal on 23 April 2002 at 0813 UTC. This region is characterized by bright sand and desert conditions. The Suez Canal is clearly observed, as is a ship in the canal near the center of the image. The DSI correctly identifies the bright regions of the image as surface features. A small amount of the bright region in the lower part of the scene was identified as cloud. The computed cloud amount for this image was 0.3%.

Summary of Cloud-Cover Analysis

The cloud analysis algorithm was designed to perform cloud-cover detection onboard the EO-1 satellite. The algorithm requires calibrated radiances, which are converted to reflectance values and processed through the cloud-cover routine to produce a cloud mask for the observed image. The routine was tested on numerous Hyperion images collected over a wide range of surface and atmospheric conditions.

The algorithm does remarkably well, considering that no thermal infrared data are available to assist in the cloud-cover determination. A set of seven tests is used to discriminate surface features from clouds. Two types of clouds are identified by this routine: low-to-mid (water) and mid-to-high (ice) clouds. Tests of the routine produced cloud-cover estimates that were generally within 5% of the visually estimated cloud-cover amount. The algorithm has the most difficulty with shadowed or darkened snow-covered surfaces that are not identified properly in the NDSI test.

Remote Sensing of Coastal Waters

Oceans comprise two-thirds of the earth surface. Remote sensing provides the only reasonable way of monitoring and understanding this majority part of

our planet. Optical properties of natural bodies of ocean water are influenced by many factors. Some of the key substances affecting ocean characteristics are phytoplankton, suspended material, and organic substances.

In general, ocean waters are partitioned into case 1 (open ocean) and case 2 (coastal) waters; case 1 waters are those in which phytoplankton are the principal agents responsible for variations in optical properties of the water. On the other hand, case 2 waters are influenced not just by phytoplankton and related par-

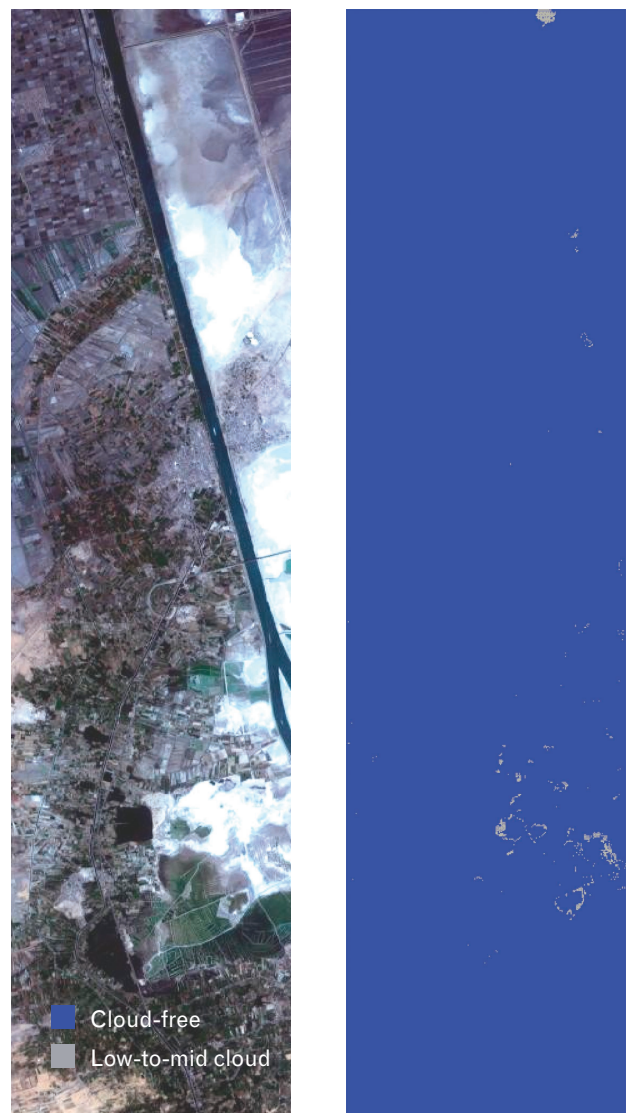


FIGURE 10. Hyperion image collected over the Suez Canal, displaying the clear conditions and bright sand characteristic of a desert scene. The algorithm computed the cloud amount for the scene to be 0.3%.

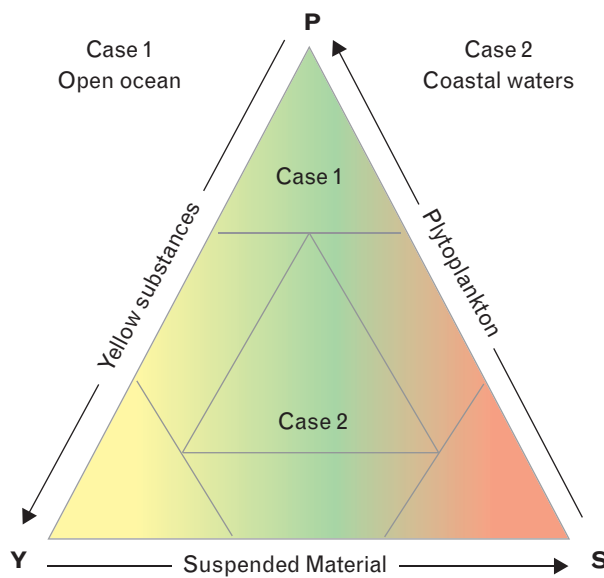


FIGURE 11. Phytoplankton (P), yellow substances (Y), and suspended material (S) are the three key contributors to the ocean color. The chart depicts the relative contributions to case 1 deep ocean and case 2 coastal waters. (Image courtesy IOCCG Report #3, 2000.)

ticles, but also by other substances, notably inorganic particles in suspension and yellow substances. Figure 11 is a representation of case 1 and case 2 waters according to their optical properties, which are primarily due to phytoplankton (P), yellow substances (Y) and suspended material (S). Coastal waters are more complex in their composition and optical properties than open ocean waters. Sensing requirements are more stringent and interpretation of data is also a challenge due to the following four important reasons [13].

First, ocean color in coastal waters is influenced in a nonlinear fashion by a number of constituents in the water. In shallow waters, it is further influenced by the depth of the water column, and by the nature of the bottom. Second, some of the inherent optical properties of the constituents that influence ocean color can be similar to each other. The similarity may persist over the entire spectral range of interest, as in the case of the absorption spectra of colored dissolved organic matter and detrital particles. Similarities impede differentiation of the substances by remote sensing.

Third, the concentrations of in-water constituents have wide dynamic ranges. For example, chlorophyll-a concentration varies over several orders of magnitude,

from about 0.01 to 100 mg m⁻³. Fourth, each of the three major components of the water that influence ocean color in case 2 waters (phytoplankton, other suspended particulates and yellow substances) represents a group of substances rather than a single substance. A consequence is the variability in their optical signatures. These points all have to be kept in mind when developing algorithms for interpretation of ocean color in case 2 waters.

Looking back on the variety of ocean color sensors flown in the last twenty-five years, as illustrated in Figure 12, we notice that the bands chosen generally vary between 0.4 and 1.0 μm . These multispectral sensors vary not only in the number of bands and exact band locations, but also the bandwidths of respective bands.

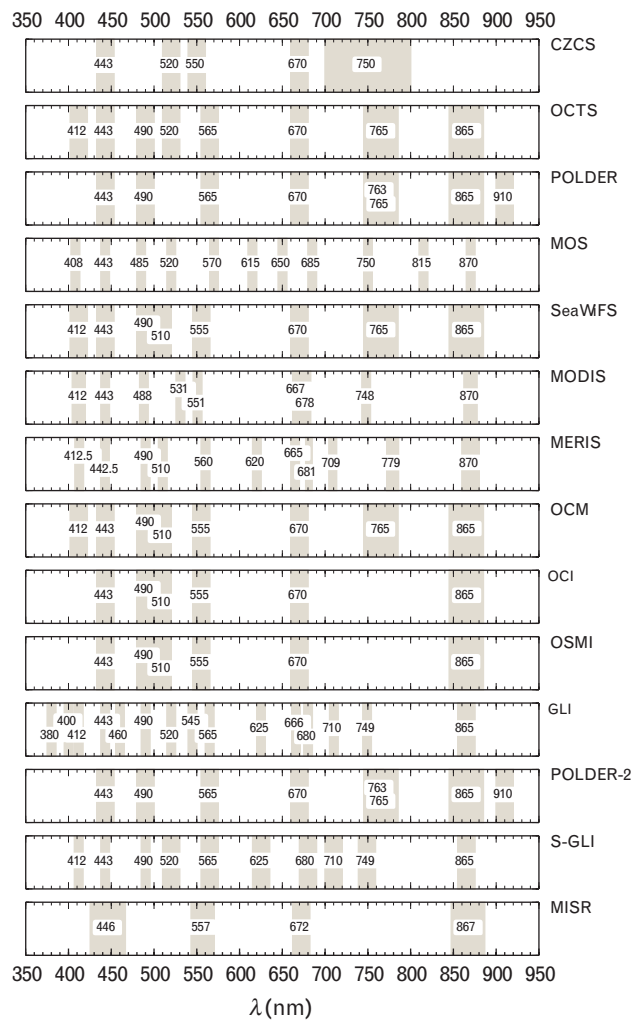


FIGURE 12. Channel distributions for a variety of ocean color sensors flown in the last twenty-five years.

The bands are chosen to utilize the reflection, backscatter, absorption, and fluorescence effects of the various species.

While ocean-product algorithms vary according to parameter and scenario, most of them are semi-empirical retrievals based on established climatological information. As previously mentioned, a challenge to coastal remote sensing is that coastal features are more complex than those of the open ocean. The small number of bands ultimately limits the extent of retrievable products. It would be of great advantage if physics-based approaches could be established as sensors with increasing number in spectral bands provide a chance to solve the complex coupled phenomena in coastal remote sensing.

To illustrate the point, we can express the top of the atmosphere reflectance of ocean as

$$R(\lambda) = T_g(\lambda) T_r(\lambda) T_a(\lambda) [R_w(\lambda) + R_s(\lambda)] + R_r(\lambda) + R_a(\lambda),$$

where T_r and T_a are atmospheric transmission factors due to Rayleigh scattering and aerosol scattering, respectively; T_g is the atmospheric gas transmittance; R_w is the water reflectance; R_s is the reflectance of the skylight and direct sunlight from the water surface; and R_r and R_a are the atmospheric path reflectance due to Rayleigh scattering and aerosol scattering, respectively [14].

Coupled effects can potentially be best resolved with hyperspectral imagery. To begin with, a hyperspectral sensor covering the spectral range between 0.4 and 1 μm has all the bands necessary to provide legacy with previous sensors and explore new information. Furthermore, most ocean characterization algorithms utilize water-leaving radiance. The atmospheric aerosol effect is most pronounced in the shortwave visible where ocean color measurements are made. With contiguous spectral coverage, atmospheric compensation can be done with more accuracy and precision.

EO-1 Data from Chesapeake Bay

To demonstrate the potential value of Hyperion data (and hyperspectral imaging in general) to coastal characterization, we analyzed EO-1 data from Chesapeake Bay from 19 February 2002. Both ALI and Hyperion



FIGURE 13. Chesapeake Bay EO-1 data from the Advanced Land Imager (ALI) and Hyperion. The selected area for analysis was approximately $6 \times 15 \text{ km}^2$ in size. These two red-green-blue composite images look nearly identical. Spectral bands between 0.43 and 0.93 μm were also used for this study, six from ALI and fifty from Hyperion.

data were available. A common area was selected for analysis. This area, approximately 6 km wide by 15 km long, consists of land, a marsh, a sand bar, and shallow water. Figure 13 shows the coastal images of ALI and Hyperion from the data set. The three-channel RGB composite images from ALI and Hyperion look practically identical. For further analysis, spectral data between 0.43 and 0.93 μm were utilized; this spectral range covers six bands from ALI and fifty bands from Hyperion. Figure 14 is the nautical chart from Chesapeake Bay with an enlarged view of the data area.

To compare the ALI and Hyperion data and to illustrate the dimensionality of data with complex features, we applied the minimum noise fraction (MNF) algorithm to both ALI and Hyperion data sets. Image reconstruction was then accomplished by inverting the transformation matrix. The reconstructed image was compared to the original image to gain insight

into the feature space and the extent of the noise in the data. Results are shown in the next section.

Feature Extraction and Information Content

Multispectral and hyperspectral images are amenable to spectral transformations that generate new sets of image components. The transformed image could make evident features not discernible in the original data or, alternatively, it might be possible to preserve the essential information content of the image with a reduced number of the transformed dimensions.

Principal-component analysis uses a linear transformation to translate and rotate multiband data into a new coordinate system that maximizes the variance. This technique is used to decorrelate data and maximize the information content in a reduced number of features [15]. The covariance matrix is first computed over the pixel spectra contained in the hyperspectral data cube of interest. Eigenvalues and eigenvectors are then obtained for the covariance matrix Σ , as given below:

$$\Sigma = E \left\{ (\mathbf{X} - \mathbf{X}_m)(\mathbf{X} - \mathbf{X}_m)^T \right\} = \Phi \Lambda \Phi^T,$$

where \mathbf{X} represents the spectral vector data, \mathbf{X}_m is the mean spectral vector over the data cube, and E is the average operator over the entire data cube. Φ is a matrix consisting of columns of eigenvectors, and Λ is a diagonal matrix of eigenvalues.

With the eigenvectors as a new coordinate system, the hyperspectral data cube is then transformed into principal components, also called eigenimages. These components are ranked in descending order of the eigenvalues (image variances). The eigenimages associated with large eigenvalues contain most of the information, while the eigenimages associated with small eigenvalues are dominated by noise. Thus a principal-component transformation allows for the determination of the inherent dimensionality and segregation of noise components of the hyperspectral image data.

The MNF transform is essentially two cascaded

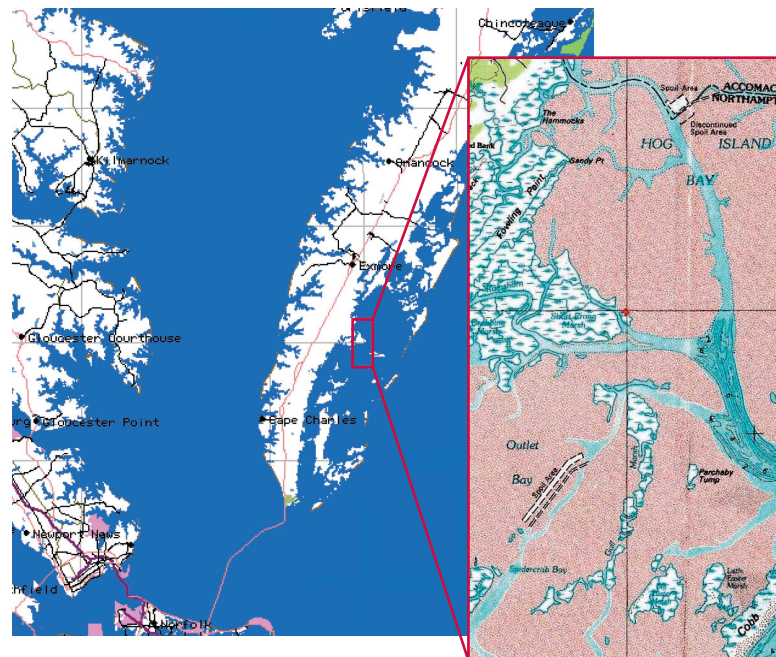


FIGURE 14. Location of EO-1 data on nautical charts of Chesapeake Bay.

principal-component transformations [16, 17]. The first transformation, based on an estimated noise covariance matrix, decorrelates and rescales the noise in the data. This first step results in transformed data in which the noise has unit variance and no band-to-band correlations. The second step is a standard principal-component transformation of the noise-whitened data. The transformed data can be divided into two parts; one part is associated with large eigenvalues and coherent eigenimages, and a complementary part is associated with near unity eigenvalues and noise-dominated images. The associated eigenvalue of each eigenimage represents the signal-to-noise ratio (SNR). The inherent dimensionality of the data can be determined from the number of coherent eigenimages, based on the quantitative SNR. By using the coherent eigenimages, we can implement an inverse MNF transformation to remove noise from data.

MNF transforms were applied to both ALI and Hyperion data. Figure 15 shows the results. Since only six ALI bands are used, six MNF components are obtained; for Hyperion there are more MNF components. We observe that the first few components compare closely with one other. For the fifth and sixth components, ALI component images are progressively

more dominated by noise, while Hyperion component images suggest more features are present. Beyond the sixth component of the Hyperion data, the eighth and ninth component images, for example, still show discernible features.

We recognize that the SNR for the Hyperion data is inferior to that for ALI data. However, this exercise demonstrates that the increased spectral coverage more than makes up for the low SNR, and that Hyperion data could be potentially useful for coastal characterization.

Owing to the information compression properties of the principal-component transformation, it lends itself to reduced representation of image data with reduced noise. Figure 16 shows the results of Hyperion image reconstruction. Both the fifth and the ninth components are used for reconstruction and compared to the original image. The six-component reconstruction clearly shows a sharper image compared to the original, indicating the reduced noise level. However, by comparing the six-component reconstruction to the nine-component reconstruction, we find additional features in the nine-component image that were clearly not present in the six-component image.

This quick comparative analysis illustrates the potential utility of high-dimensional hyperspectral data compared to multispectral data, even when SNR is less favorable. Also, transformation of the image data allows us to enhance the image quality by removing noise components and making features more distinguishable.

Retrieval of Chlorophyll

We describe the retrieval of chlorophyll-a as an example of Hyperion data applications for coastal ocean waters. Chlorophyll-a absorbs relatively more blue and red light than green, and the spectrum of backscat-

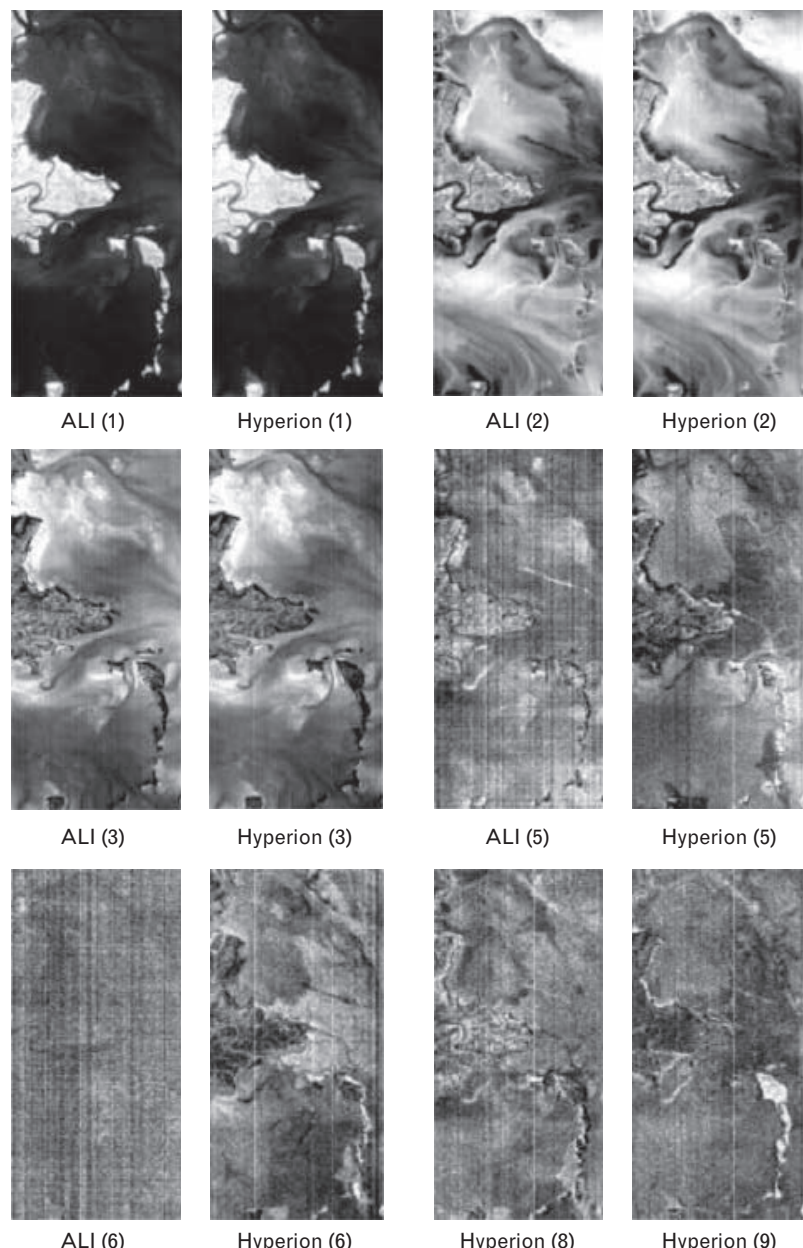


FIGURE 15. Comparison of six minimum noise fraction (MNF) components from ALI and Hyperion.

tered sunlight or color of ocean water progressively shifts from deep blue to green as the concentration of phytoplankton increases. A large data set containing coincident *in situ* chlorophyll and remote-sensing reflectance measurements was used to evaluate a wide variety of ocean color chlorophyll algorithms for use by the Sea-Viewing Wide Field-of-View Sensor (SeaWiFS) [18]. Two types of algorithms—empirical and semi-analytical—were extensively reviewed. It was

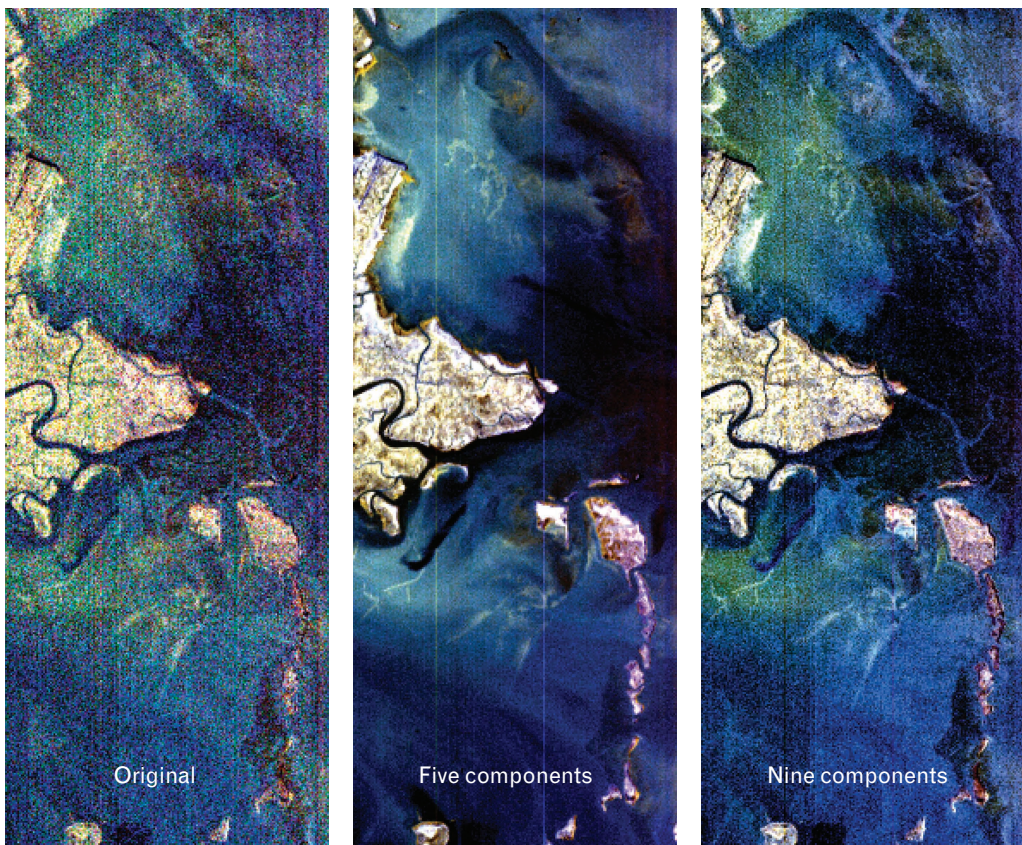


FIGURE 16. Original Hyperion image (left); reconstructed images from the inverse MNF algorithm using five components (center) and nine components (right). The false-color selection (red is from the 440 to 550 nm band, green is from the 490 to 550 nm band, and blue is from the 530 to 550 nm band) is based on spectral bands commonly used for ocean color characterization.

concluded that ocean chlorophyll (OC)-2 and OC-4 are the two best estimators. Improved performance was obtained with the OC-4 algorithm, a four-band (443, 490, 520, and 555 nm), maximum-band-ratio formulation.

Before applying the OC-4 algorithm to the Chesapeake Bay data, we first used a standard atmospheric correction algorithm to obtain the surface reflectance. The land mass was also masked out. Figure 17 shows the resultant chlorophyll concentration map, with white representing the lowest value. Quantitative values are plotted for selected horizontal lines as well.

Fortunately, supporting data can be used as “surrogate” ground truth. The first data set, shown in Figure 18, came from routine low-altitude aircraft data collected on 19 February 2002 from the Chesapeake Bay Remote Sensing Program [24]. The second data set, shown in Figure 19, was taken from the pub-

lished weekly SeaWiFS products for the week of 18 to 25 February 2002 [25]. All derived values from the various measurements are consistent, and in the range from 2 to 4 mg/m³. Certainly much more work remains to be done to validate the application of Hyperion data to coastal ocean waters. This initial result, however, is very encouraging.

Summary of Coastal Water Analysis

EO-1 data gathered from Chesapeake Bay on 19 February 2002 are analyzed to demonstrate the potential value of Hyperion data (and hyperspectral imaging in general) to coastal characterization. We first illustrate that hyperspectral data inherently provide more information for feature extraction than multispectral data, despite the fact that Hyperion has higher SNR than ALI. Chlorophyll retrievals from Hyperion data compare favorably with data from other sources.

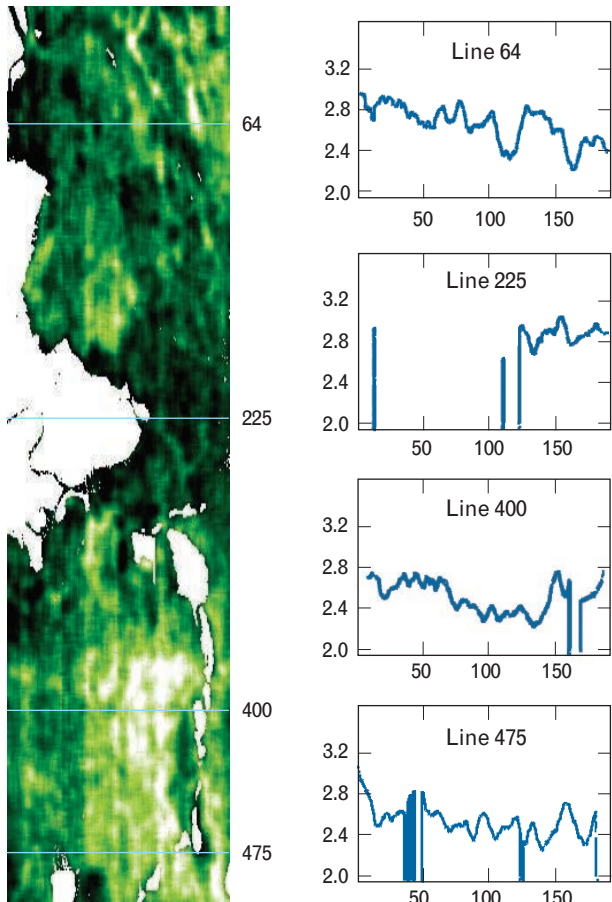


FIGURE 17. Chlorophyll-a retrieval results from the Sea-Viewing Wide Field-of-View Sensor (SeaWiFS) ocean chlorophyll (OC)-4 algorithm. In the chlorophyll concentrations map on the left, white represents the lowest value and black represents the highest value. The four plots on the right show quantitative concentration values of selected horizontal lines in the concentration map.

Terrestrial Analysis Applications

To demonstrate the utility of EO-1 data, we conducted an analysis of combined panchromatic, multispectral (ALI), and hyperspectral (Hyperion) data. In particular, we describe the value added to hyperspectral imaging data with additional spectral information [19].

As described earlier, Hyperion is a push-broom imaging spectrometer. Each square pixel subtends a ground sampling distance of 30 m, is sampled every 30 m, and measures a complete spectrum from 0.4 to 2.5 μm in 220 spectral channels. Each image covers a ground area of 7.65 km by 185 km, as illus-

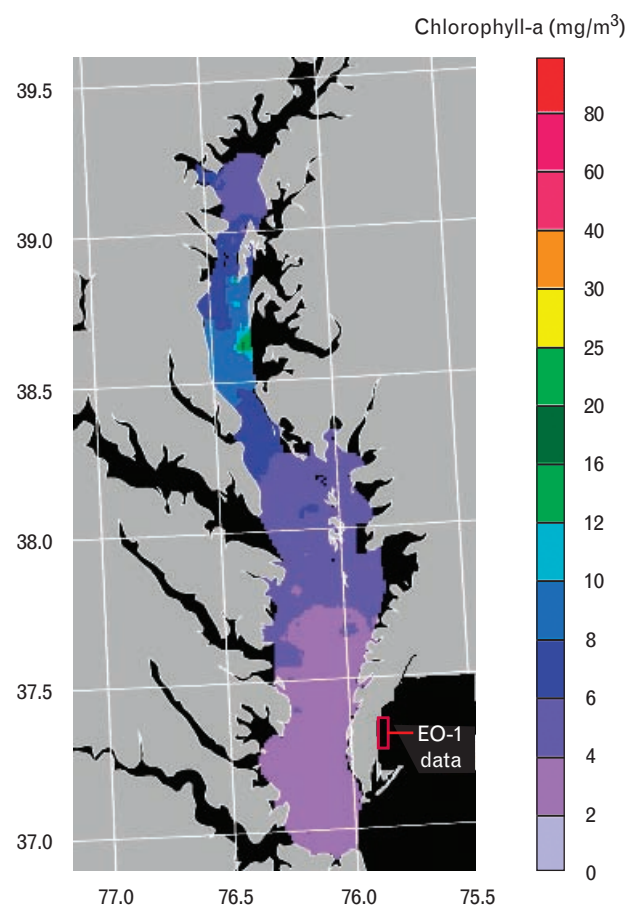


FIGURE 18. Supporting data from the Chesapeake Bay Remote Sensing Program (CBRSP). Chlorophyll-a data is estimated from a SeaWiFS Aircraft Simulator instrument over a well-maintained ground site, and published in a Chesapeake Bay web site. The Chlorophyll-a immediately inside the bay is between 2 to 4 mg/m³. The red box delineates the area of the EO-1 data. The flight schedule is about twice a month, at a measurement altitude of 500 ft. In this case the measurements were taken the same day as the Hyperion data, on 19 February 2002. The picture in the figure is reproduced from the CBRSP web site.

trated previously in Figure 1. The ALI is a co-incident multispectral imaging sensor also onboard EO-1. ALI, whose spectral bands are listed in Table 3, covers a larger area (37 km swath width) with the same spatial resolution but in nine broad bands. The area covered by ALI overlaps approximately 80% with that of Hyperion. In addition, ALI has a high-resolution panchromatic band of 10 m pixel resolution, which is three times better than that of the ALI multispectral imaging sensor and the Hyperion hyperspectral imaging sensor. The purpose of this section is to demon-

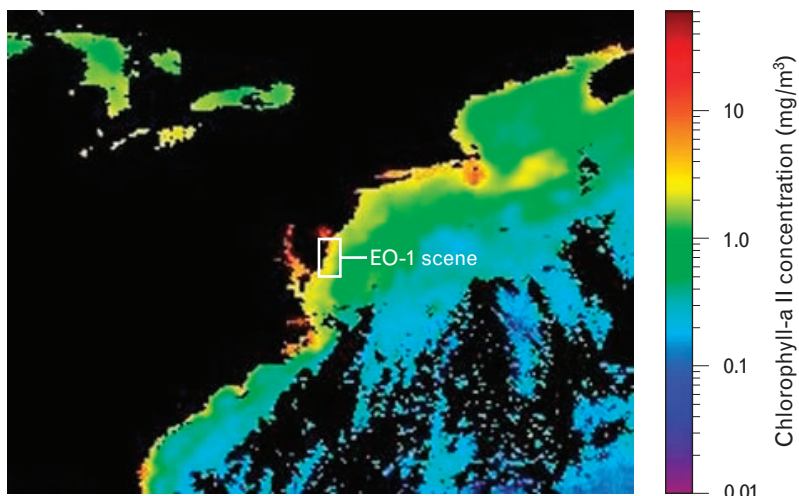


FIGURE 19. SeaWiFS data averaged for the week 18 February to 25 February 2002. SeaWiFS products are published regularly on a NASA web site. The calculated values of chlorophyll-a are from 2.0 to 4.0 mg/m³.

strate the utility of a combined analysis of EO-1 panchromatic, multispectral, and hyperspectral data.

Data sets from Coleambally Irrigation Area, Australia, on 7 March 2000, and San Francisco Bay area on 17 January 2000 are analyzed. Atmospheric correction is first applied to the radiance data [20]. Hyperion and ALI data over the Coleambally Irrigation Area, Australia, are used for terrain characterization in terms

of soil moisture content and vegetation status. Hyperion data are also subject to spectral unmixing to illustrate sub-pixel analysis. Abundance levels of lush vegetation and bare soil are estimated for image pixels in different fields of crops. Anomaly detection algorithms are applied to Hyperion image data of the San Francisco Bay area. Detections from Hyperion data are compared with previous Airborne Visible/Infrared Imaging Spectrometer (AVIRIS) data and known library spectra for material identification. Panchromatic-sharpened ALI imagery is also shown for enhanced visualization of spatial features.

Terrain Characterization

Vegetation status and soil moisture content are two major factors contributing to terrain characterization. As an example, EO-1 data from the Coleambally Irrigation Area, consisting both of bare soil and various types of vegetation, are used to illustrate applications of terrain characterization. Simultaneous multispectral and hyperspectral data are also compared.

In the vegetation spectra shown in Figure 20, we

Table 3. ALI Spectral Bands

Spectral Band	Wavelength (μm)	Ground Sampling Distance (m)
Panchromatic	0.48–0.69	10
1p	0.43–0.45	30
1	0.45–0.52	30
2	0.53–0.61	30
3	0.63–0.69	30
4	0.78–0.81	30
4p	0.85–0.89	30
5p	1.20–1.30	30
5	1.55–1.75	30
7	2.08–2.35	30

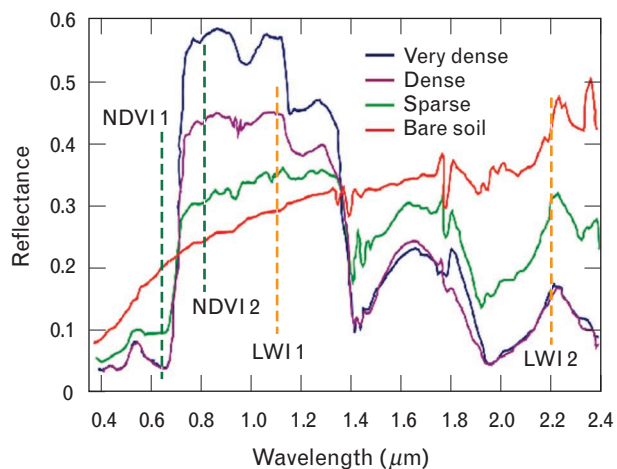


FIGURE 20. Sample vegetation and soil spectra. The normalized difference vegetation index (NDVI) measuring spectral differences around the red edge is commonly used to represent the health and amount of vegetation. The liquid water index (LWI) estimates water content on the basis of reflectance differences between 1.1 μm and 2.2 μm .

observe a decrease in the radiance at $0.68 \mu\text{m}$ and a large increase at near infrared, since chlorophyll in the vegetation absorbs visible light from the sun, and reflects the infrared radiation. The normalized difference vegetation index (NDVI) measuring spectral differences around the red edge is commonly used to represent the health and amount of vegetation.

$$\text{NDVI} = \frac{\rho(0.86 \mu\text{m}) - \rho(0.66 \mu\text{m})}{\rho(0.86 \mu\text{m}) + \rho(0.66 \mu\text{m})},$$

where $\rho(0.66 \mu\text{m})$ and $\rho(0.86 \mu\text{m})$ are reflectances at $0.66 \mu\text{m}$ and $0.86 \mu\text{m}$, representing red and near-infrared band reflectance, respectively.

Under smoky or cloudy conditions, both obscurants tend to mask the underlying signal at visible and near-infrared wavelengths [21]. However, information identifying vegetation can be retrieved from spectral channels at longer wavelengths, which are transmitted through some smoke. The liquid water index (LWI) estimates water content based on reflectance differences between $1.1 \mu\text{m}$ and $2.2 \mu\text{m}$:

$$\text{LWI} = \frac{\rho(1.1 \mu\text{m}) - \rho(2.2 \mu\text{m})}{\rho(1.1 \mu\text{m}) + \rho(2.2 \mu\text{m})}.$$

A comparison of the spectral characteristics of the channels used in the LWI ($1.1 \mu\text{m}$ and $2.2 \mu\text{m}$) and those used for the NDVI ($0.66 \mu\text{m}$ and $0.86 \mu\text{m}$) shows similar but reversed trend between dense and sparse or no vegetation conditions (see Figure 20). While NDVI captures the state of vegetation via chlorophyll content, LWI is indicative of the liquid water content in the vegetation. Therefore, it is not surprising that LWI, like NDVI, has the capability to discriminate between vegetation conditions, but with the added benefit of operating under obscured conditions.

Another index based on Landsat 7 ETM+ bands 5 and 7 is the soil moisture index (SMI) [22]:

$$\text{SMI} = \frac{\rho(1.55 - 1.75 \mu\text{m})}{\rho(2.08 - 2.35 \mu\text{m})}.$$

These indices are calculated for the Coleambally image with both Hyperion and ALI data. ALI bands closest to the wavelengths indicated in the index formulas are used. Multispectral bands 3 and 4p are employed for NDVI, and bands 5p and 7 are employed for LWI. For comparison, Hyperion spectral data are averaged over the bandwidth of corresponding ALI bands before index calculation. Figure 21 shows line profiles of

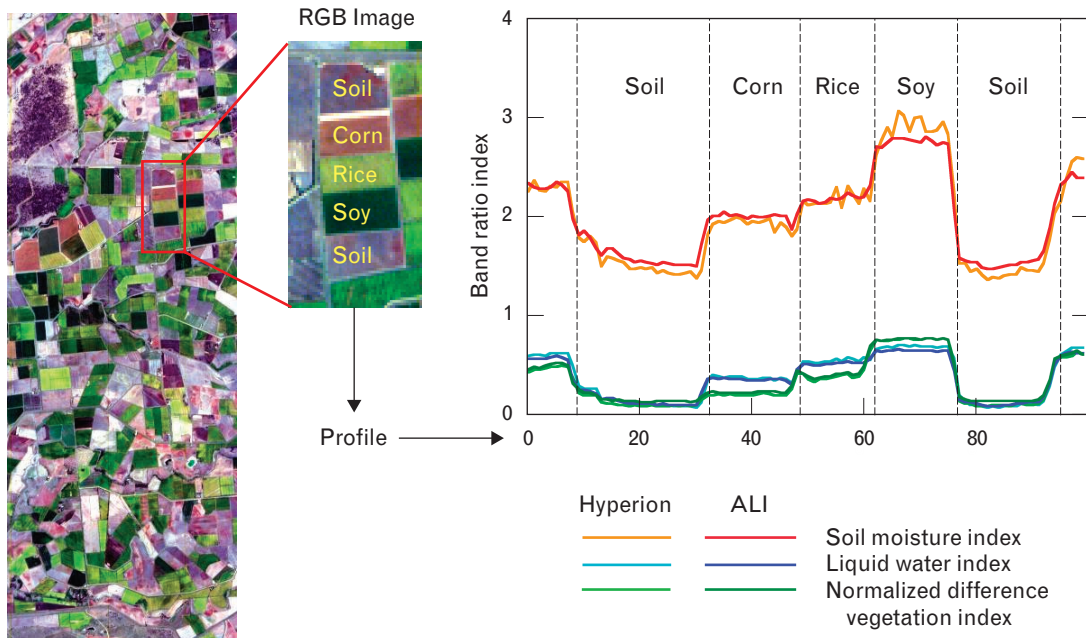


FIGURE 21. Line profiles of NDVI, LWI, and the soil moisture index (SMI) over areas of soil, corn, rice, soybean, and a second plot of soil. The LWI profile appears to closely follow the NDVI profile, except for some small deviations. The SMI profile also resembles the NDVI profile in overall shape but has a different scale.

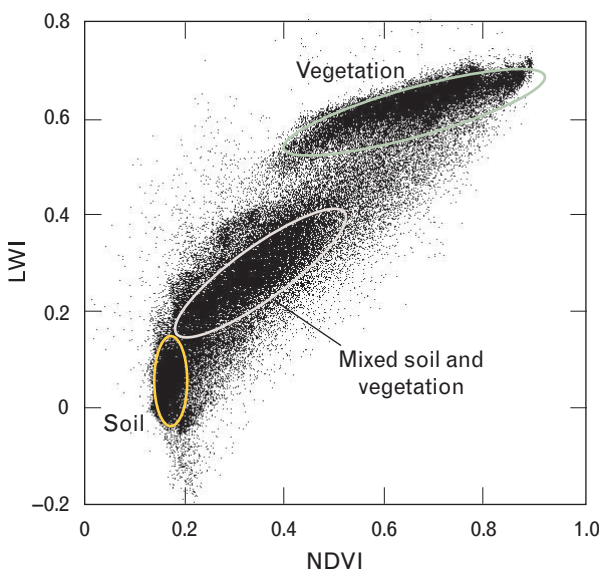


FIGURE 22. Scatter plot of LWI and NDVI derived from Hyperion data over Coleambally. Separate clusters can be delineated from this index plot. The cluster at the lower left consists of data from soil. Some spread in the LWI dimension is seen, which indicates different levels of moisture content in the soil. The cluster at the top represents data from vegetation and has a larger response in NDVI than in LWI.

NDVI, LWI, and SMI over areas of soil, corn, rice, and soybean in the image. The LWI profile appears to closely follow the NDVI profile, except for some small

deviations. The SMI profile also resembles the NDVI profile in overall shape but has a different scale, since it is calculated as a band ratio rather than a normalized band difference like the NDVI and LWI. The indices are high at the soybean area, which indicates the most lush condition, and low at the two soil areas where there is little or no vegetation. By comparing the profiles derived from Hyperion and ALI data, we can see that the two sets are nearly identical, although some noise is apparent from pixel to pixel in the profiles derived from Hyperion data.

To further examine the correlations between LWI and NDVI, we plot the indices derived from Coleambally Hyperion data in a scatter plot, as shown in Figure 22. Separate clusters can be delineated from the index plot because of various LWI-NDVI correlations of different material. The cluster located at lower left—low LWI and NDVI less than 0.2—consists of data from soil. In this region, there is little change in NDVI. Some spread in the LWI dimension is seen, which indicates different levels of moisture content in the soil. The cluster in the middle extends LWI values from approximately 0.15 to 0.45 and NDVI from 0.2 to 0.5. This cluster represents pixel data with mixtures of soil and vegetation. The cluster at the top represents data from vegetation and has a larger extent in NDVI

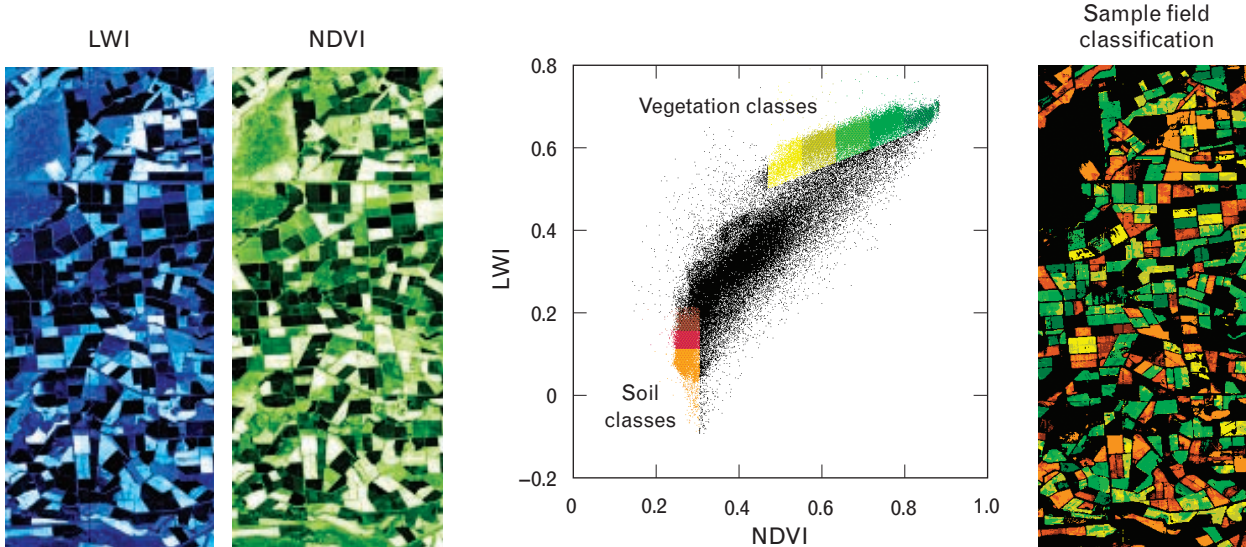


FIGURE 23. Soil and vegetation clusters in the scatter plot are divided into eight regions. Regions colored in orange, light sienna, and dark sienna represent soil classes, while regions colored in five shades from yellow to dark green represent vegetation classes. Image pixels contributing to the various regions defined in the scatter plot are mapped with the corresponding colors into the field classification image on the right. The areas not mapped are mostly mixtures of soil and vegetation.

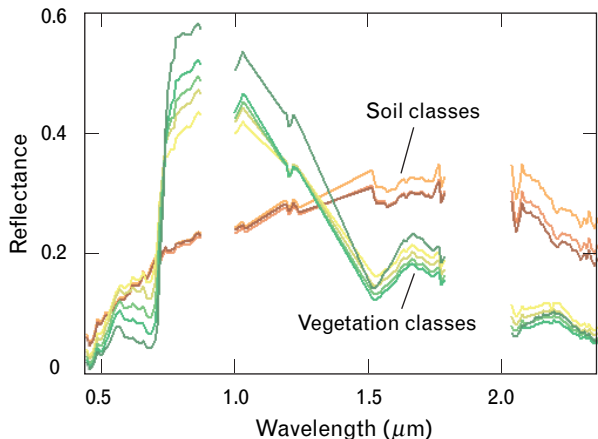


FIGURE 24. Mean reflectance spectra of the eight soil and vegetation regions shown in Figure 23. The soils with less moisture content have higher reflectance in SWIR (1 to 2.5 μm). In the vegetation spectra, the different changes of reflectance between 0.66 μm and 0.86 μm agree well with the NDVI values defined for the regions.

than in LWI. This extent indicates that LWI, while strongly correlated with NDVI, is less sensitive to vegetative state than the vegetation index. Reexamination of Figure 21 in this light reinforces this conclusion, as deviations from 0.5 in the index are more exaggerated by NDVI than by the LWI.

The soil and vegetation clusters are further divided into smaller regions to observe the progressive change in spectral characteristics, as shown in Figure 23. The regions colored in orange, light sienna, and dark sienna represent soil, while five shades from yellow to dark green represent vegetation conditions. Image pixels contributing to the various regions defined in the Figure 23 scatter plot are mapped with corresponding colors in the field classification image on the right. Most mapped fields are monochromatic or dichromatic, representing certain soil or vegetation status, and not a random mixture of several colors. This result indicates these fields are relatively uniform. The areas not mapped are mostly mixtures of soil and vegetation.

Different fields in the Coleambally Irrigation Area are characterized by moisture content and vegetation status. The mean spectra of the eight different regions are plotted in Figure 24. The soil with less moisture has a higher reflectance in SWIR (1 to 2.5 μm). In the vegetation spectra, the different changes of reflectance between 0.66 μm and 0.86 μm agree well with the

NDVI values defined for the regions. Dividing the entire LWI-NDVI space given in the scatter plot allows for effective characterization of the fields.

Spectral Unmixing

The pixel resolution of both the Hyperion hyperspectral sensor and the ALI multispectral sensor is 30 m on the ground. If there are different types of material in the pixel, each contributes to the combined spectral measurement. By assuming linear combinations of M types of material, and each material occupies a fraction a_m of the pixel, the pixel spectrum ρ_T can be written as

$$\rho_T = \sum_{m=1}^M a_m \rho_m,$$

where m represents the material type, $0 \leq a_m \leq 1$, $\sum a_m = 1$, and a_m is the different fraction of each material m within the pixel.

Given the contributing materials, the material abundance in a pixel can be recovered from hyperspectral data with various least-squared-error unmixing algorithms [23]. An unmixing algorithm is unconstrained when the fractions are not limited to the conditions of $0 \leq a_m \leq 1$ and $\sum a_m = 1$.

Figure 25 shows sample areas of soybean and soil in the Coleambally image. Regions of interest are selected as shown on the Hyperion image to include a lush vegetative area in the soybean field and a bare region in the soil area. The right side of Figure 25 shows the mean spectra of the regions, which are used to demonstrate a two-class unmixing analysis of lush vegetation and bare soil. The unconstrained least-squares unmixing algorithm is applied to the image. The left side of Figure 26 shows the retrieved soybean and soil abundances. The right side of Figure 26 shows the abundance values of pixels at the horizontal line indicated in the abundance images. Results show 100% soybean for samples 15 to 20, mixtures of soybean and soil for samples 21 to 34, 100% soil for samples 35 to 42. The abundance of soybean decreases progressively from left to right while soil increases in the mixture at the transitional region. Sample number 28 appears near the middle of the transition. The abundance retrieval quantifies the amount of soybean and bare soil in the transitional region. This process illustrates how an un-

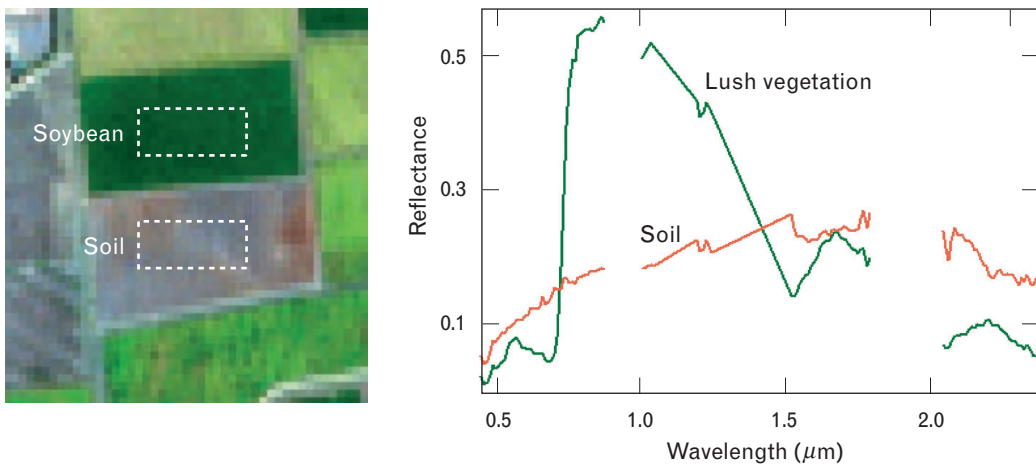


FIGURE 25. Sample areas of soybean and soil in the Coleambally image. Regions of interest are selected on the Hyperion RGB image shown on the left to include a lush vegetative area in the soybean field and a bare region in the soil area. On the right are the mean reflectance spectra of the regions, which are used to demonstrate a two-class unmixing analysis of lush vegetation and bare soil.

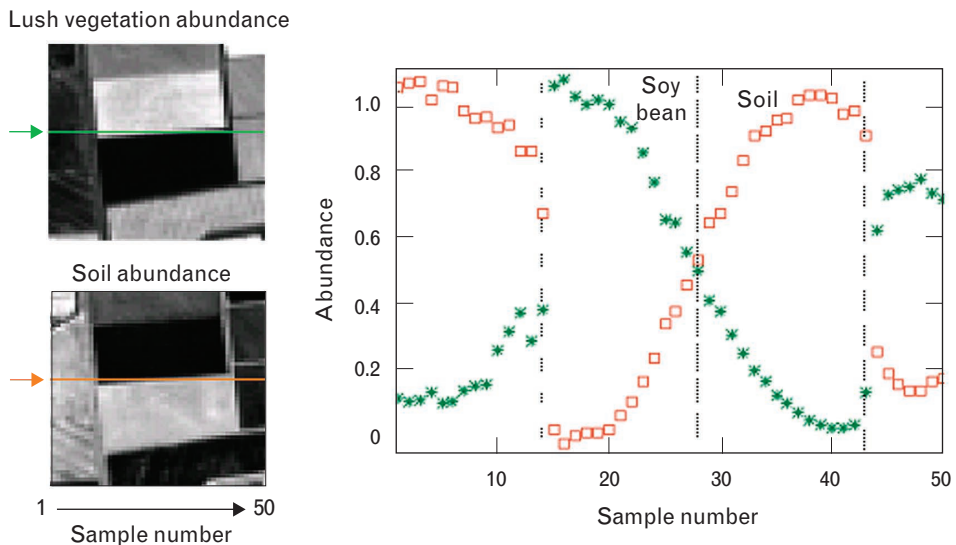


FIGURE 26. Retrieved soybean and soil abundance profiles from the Hyperion data. The plot shows abundances for pixels at the indicated horizontal line of the two images. The abundance of soybean decreases progressively from left to right, while soil increases in the mixture at the transitional region. Sample number 28 appears near the middle of the transition.

mixing algorithm can be applied to hyperspectral data to obtain quantitative information of different materials in a given pixel.

Spectral Feature Analysis

Hyperion data were collected over San Francisco Bay on 17 January 2000. An AVIRIS collection over the same area, taken on 20 June 1997, is used here for comparison with Hyperion. Some common features,

such as water, runway, and grass, are selected for comparison. The Atmosphere Removal (ATREM) algorithm [20] was first applied to both data sets for atmospheric compensation to reduce the data to spectral reflectance values. As shown in Figure 27, spectral features from both data sets appear very similar, except that the retrieved surface reflectance values from the Hyperion data appear lower at all wavelengths.

The MNF transformation [17] algorithm is then

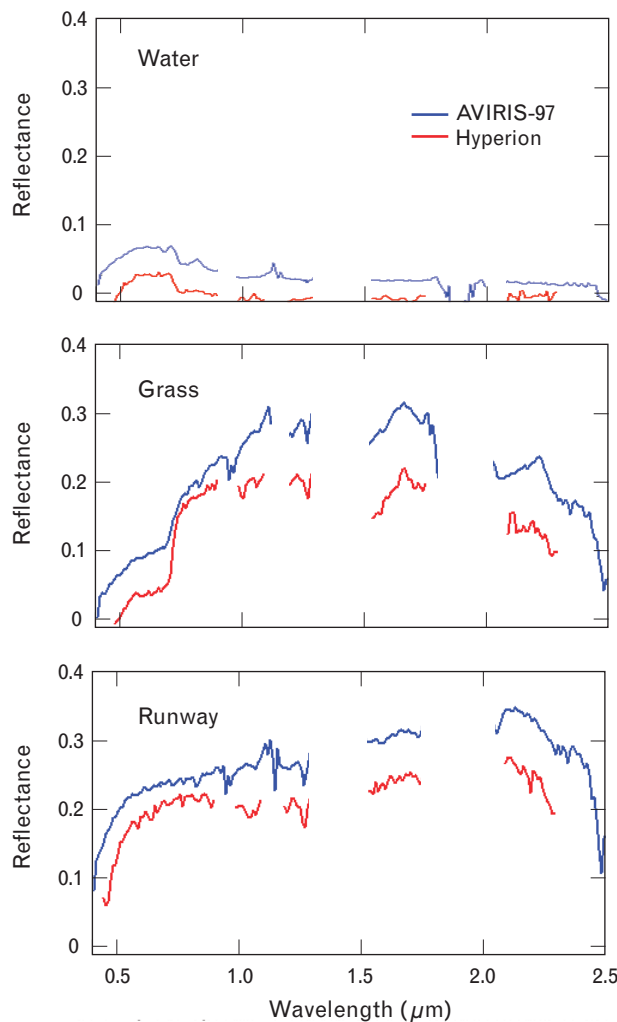


FIGURE 27. Retrieved surface reflectance from the Atmospheric Removal (ATREM) algorithm applied to Hyperion and Airborne Visible/Infrared Imaging Spectrometer (AVIRIS) data for selected features. Hyperion and AVIRIS data appear similar in overall spectral shapes, except that the Hyperion data are consistently lower in their reflectance signatures.

applied for further feature extraction. Clusters of anomalous pixels are detected in the tenth Hyperion component. Analysis of the AVIRIS data also found anomalies detected at the same location as in the Hyperion data. Figure 28 shows these images, with the common detection in the red circle in the ALI image. The high-resolution panchromatic-band sharpened ALI image in the figure shows similar spatial features as the AVIRIS image at the detection. (Note: AVIRIS spatial resolution is 20 m.) Figure 29 shows spectral signatures of the detections from both Hyperion and AVIRIS data.

Figure 30 shows a photograph of the building at the detected site. The detections in the Hyperion hyperspectral data appear to be of the blue roofing material of the building. For verification, three panels of sample material similar to the blue roofing material were acquired and measured with a hand-held spectrometer. The spectral signatures of the sample roof panels are plotted together with the detected data from both Hyperion and AVIRIS images, as shown in Figure 31.

Terrestrial Analysis Summary

Examples of Hyperion data applications are shown for terrain characterization, spectral unmixing, and anomaly detection. For terrain characterization, various simple indices are used to characterize the soil and vegetation conditions. They include the normalized difference vegetation index (NDVI), the liquid water index (LWI), and the soil moisture index (SMI). Consistent results were demonstrated between Hyperion and ALI. These indices were further used to map the bare and vegetated fields, with promising results. For spectral unmixing, some adjacent fields with distinctly different materials (soil and verdant soybean) were used for subpixel analysis. The results illustrate how unmixing algorithms can be applied to hyperspectral data to obtain quantitative abundance information of the materials contained in a given pixel.

The Hyperion data from San Francisco Bay were used first to compare with AVIRIS data collected some two and a half years earlier. Anomaly detection algorithms were then applied to both data sets. A building complex with distinct roof material was detected with both images. Subsequently, samples of similar roof panels were acquired and their spectral signatures were measured with a hand-held spectrometer, corroborating the detections by both Hyperion and AVIRIS.

Summary

This article describes three examples that demonstrate the utility of the EO-1 Hyperion sensor data in different applications: cloud-cover analysis, coastal water feature extraction, and terrestrial analysis applications.

Cloud-cover analysis deals primarily with the problem of discrimination of clouds from surface features. A simplified cloud detection algorithm was developed that utilizes only six bands in reflected solar measure-

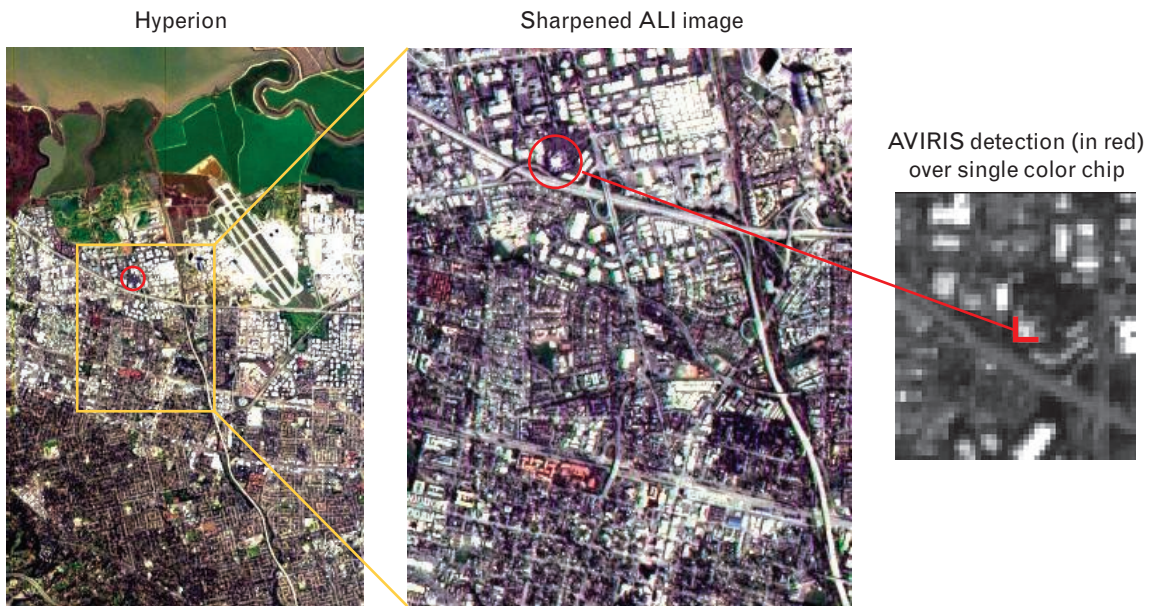


FIGURE 28. Anomaly detections in Hyperion and AVIRIS data. The high-resolution panchromatic-band sharpened ALI image shows spatial features similar to the AVIRIS image at the detection.

ments from the EO-1 Hyperion sensor to discriminate clouds from all other features in the image. The selection of the six bands provided spectral information at critical wavelengths, while keeping processing costs to a minimum, because onboard computer memory and processing time are both limited for this intended application. The cloud-cover detection process was applied to a set of twenty Hyperion scenes with varying

cloud cover, cloud type, surface characteristics, and seasonal collection times.

Coastal-water feature-extraction analysis was performed on EO-1 data recorded over Chesapeake Bay on 19 February 2002 to demonstrate the potential value of Hyperion data to coastal characterization. Spectral applications for ocean waters were briefly discussed. EO-1 data from both the ALI multispectral

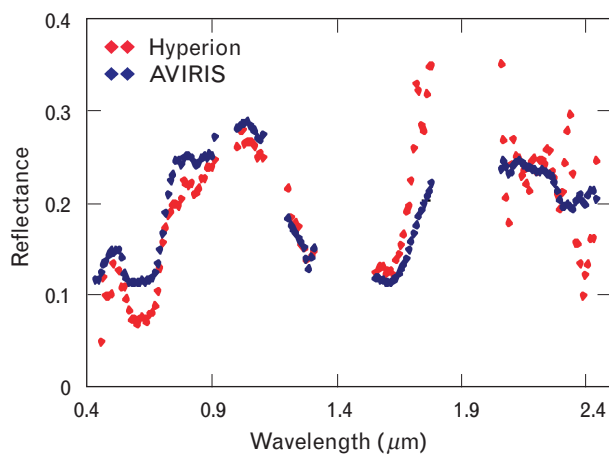


FIGURE 29. Spectral reflectance signatures of anomaly detections from Hyperion and AVIRIS data. The detections appear similar in spectral shapes to a specific type of paint in our spectral library.



FIGURE 30. Photograph of building at the detected site. The anomaly detections in the hyperspectral data shown in Figure 29 appear to be caused by the blue roofing material of the building.

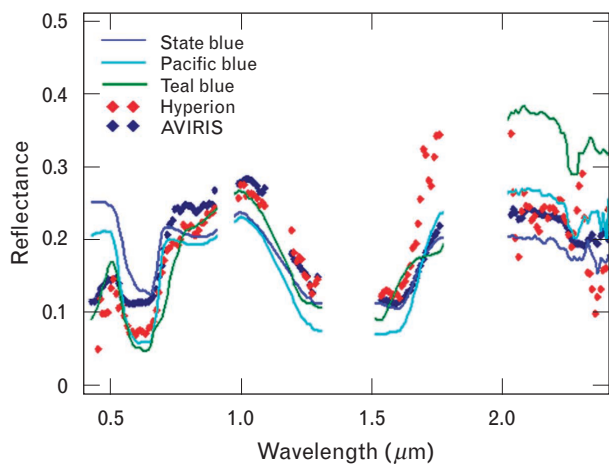


FIGURE 31. Spectral reflectance signatures of three different colored roof panels, plotted with the detected data from Hyperion and AVIRIS images. The signatures compare well in overall shape.

sensor and the Hyperion hyperspectral sensor were compared to establish the relative quality and additional feature-extraction potential for Hyperion data. Chlorophyll retrieval was carried out by using an existing simple algorithm. The results compared favorably with data from other satellite and aircraft sources.

Application examples are also shown for terrain characterization, spectral unmixing, and anomaly detection. Data sets from Coleambally Irrigation Area, Australia, on 7 March 2000 and the San Francisco Bay area on 17 January 2000 were employed for the analysis. Soil and vegetation properties such as soil moisture, vegetation chlorophyll, and plant liquid water were explored to characterize various agriculture fields. Spectral unmixing, feature extraction, and anomaly detection algorithms were also applied for different applications.

In each of the applications considered we demonstrated that hyperspectral data can provide utility; in some cases this was done by using only a few selected bands, while in other cases this was done by exploring full spectral information. The ultimate strength of hyperspectral remote sensing is exactly its versatility in data use; simple band thresholds, ratios, and differences are used to take advantage of known phenomenology. Signal processing approaches, such as anomaly detection and matched filtering algorithms, take advantage of the full spectral data such that subtle dif-

ferences can be explored. This article highlights both approaches and illustrates a variety of applications for Hyperion data.

Acknowledgments

This work was part of the Hyperspectral Technology Assessment Program (HTAP) sponsored by the Deputy Under Secretary of Defense for Science and Technology. The authors wish to express their gratitude to Capt. Frank Garcia and Lt. Col. Karl Dahlhauser for their support.

Part of the work (cloud-cover analysis) was sponsored by the NASA EO-1 Extended Mission program. We want to thank Bruce Trout at Microtel and Dan Mandl, Jerry Miller, Stuart Frye, and Lawrence Ong at NASA Goddard Space Flight Center for their interactions throughout this program, and Steve Ungar of NASA, EO-1 project scientist, for his initial support of the cloud-cover effort.

Another portion of the work (coastal characterization) is also part of the NOAA Geostationary Operational Environmental Satellite (GOES) program conducted at Lincoln Laboratory and sponsored by NOAA National Environmental Satellite, Data and Information Service (NESDIS). The authors wish to acknowledge the guidance from—and valuable discussions with—Edward Howard and John Pereira, both of NOAA NESDIS. We also acknowledge Bijoy Misra and Kris Farrar at Lincoln Laboratory for their contributions earlier in the program.

REFERENCES

1. M.K. Griffin, H.-H.K. Burke, D. Mandl, and J. Miller, "Cloud Cover Detection Algorithm for EO-1 Hyperion Imagery," *SPIE 5093*, 2003, pp. 483–494.
2. IOCCG (1998), "Minimum Requirements for an Operational, Ocean-Colour Sensor for the Open Ocean," Reports of the International Ocean-Colour Coordination Group, No. 1, IOCCG, Dartmouth, Canada.
3. IOCCG (1999), "Status and Plans for Satellite Ocean-Colour Missions: Considerations for Complementary Missions," J.A. Yoder, ed., Reports of the International Ocean-Colour Coordination Group, no. 2, IOCCG, Dartmouth, Canada.
4. IOCCG (2000), "Remote Sensing of Ocean Colour in Coastal, and Other Optically-Complex, Waters," S. Sathyendranath, ed., Reports of the International Ocean-Colour Coordination Group, No. 3, IOCCG, Dartmouth, Canada.
5. J. Pearlman, S. Carman, C. Segal, P. Jarecke, P. Clancy, and W. Brown, "Overview of the Hyperion Imaging Spectrometer for the NASA EO-1 Mission," *2001 IGARSS 6*, Sydney, Australia, 9–13 July 2001, pp. 3036–3038.
6. <http://EO1.usgs.gov>
7. S.G. Ungar, "Overview of the Earth Observing One (EO-1) Mission," *2002 IGARSS 1*, Toronto, 24–28 June 2002, pp. 568–571.
8. S.A. Ackerman, K.I. Strabala, W.P. Menzel, R.A. Frey, C.C. Moeller, and L.E. Gumley, "Discriminating Clear Sky from Clouds with MODIS," *J. Geophys. Res.* **103** (D24), 1998, pp. 32141–32157.
9. A. Berk, L.S. Bernstein, G.P. Anderson, P.K. Acharya, D.C. Robertson, J.H. Chetwynd, and S.M. Adler-Golden, "MODTRAN Cloud and Multiple Scattering Upgrades with Application to AVIRIS," *Remote Sens. Environ.* **65** (3), 1988, pp. 367–375.
10. B.-C. Gao and Y.J. Kaufman, "Correction of Thin Cirrus Effects in AVIRIS Images Using the Sensitive 1.375- μm Cirrus Detecting Channel," *Summaries of the Fifth Annual JPL Earth Science Workshop 1*, 1995, pp. 59–62 (JPL Publication 95-1).
11. B.-C. Gao, Y.J. Kaufman, W. Han, and W.J. Wiscombe, "Removal of Thin Cirrus Path Radiances in the 0.4–1.0- μm Spectral Region Using the 1.375- μm Strong Water Vapor Absorption Channel," *Summaries of the Seventh JPL Airborne Earth Science Workshop 1*, 12–16 Jan. 1998, pp. 121–130 (JPL Publication 97-2).
12. C.J. Tucker, "Red and Photographic Infrared Linear Combinations for Monitoring Vegetation," *Remote Sens. Environ.* **8** (2), 1979, pp. 127–150.
13. H.-H.K. Burke, B. Misra, S.M. Hsu, M. Griffin, C. Upham, and K. Farrar, "EO-1 Analysis Applicable to Coastal Characterization," *SPIE 5093*, 2003, pp. 507–516.
14. S.C. Liew, "Computation of Coastal Sea Water Absorption Coefficients and Retrieval of Water Quality Parameters from EO-1 Hyperion Data," *2002 IGARSS 2*, Toronto, 24–28 June 2002, pp. 802–804.
15. J.A. Richards, *Remote Sensing Digital Image Analysis: An Introduction*, 2nd ed. (Springer-Verlag, Berlin, 1993).
16. J.W. Boardman and F.A. Kruse, "Automated Spectral Analysis: A Geological Example, Using AVIRIS Data, North Grapevine Mountains, Nevada," *Proc. ERIM Tenth Thematic Conference on Geologic Remote Sensing: Exploration, Environment, and Engineering, San Antonio, Tex.*, 9–12 May 1994, pp. I.407–I.418.
17. A.A. Green, M. Berman, P. Switzer, and M.D. Craig, "A Transformation for Ordering Multispectral Data in Terms of Image Quality with Implications for Noise Removal," *IEEE Trans. Geosci. Remote Sens.* **26** (1), 1988, pp. 65–74.
18. J.E. O'Reilly, M. Stephane, B.G. Mitchell, D.A. Siegel, K.L. Carter, S.A. Garver, M. Kahru, and C. MacClain, "Ocean Color Chlorophyll Algorithms for SeaWiFS," *J. Geophys. Res.* **103** (C11), 1998, pp. 24,937–24,953.
19. S.M. Hsu, H.-H.K. Burke, S. Orloff, and M. Griffin, "Examples of EO-1 Data Analysis," *SPIE 5093*, 2003, pp. 362–372.
20. B.-C. Gao, K.B. Heidebrecht, and A.F.H. Goetz, "Derivation of Scaled Surface Reflectances from AVIRIS Data," *Rem. Sens. Environ.* **44** (2/3), 1993, pp. 165–178.
21. M.K. Griffin, S.M. Hsu, H.-H.K. Burke, and J.W. Snow, "Characterization and Delineation of Plumes, Clouds and Fires in Hyperspectral Images," *SPIE 4049*, 2000, pp. 24–28.
22. H.B. Musick and R.E. Pelletier, "Response of Some Thematic Mapper Band Ratios to Variation in Soil Water Content," *Photogramm. Eng. Remote Sens.* **52** (10), 1986, pp. 1661–1668.
23. N. Keshava and J.F. Mustard, "Spectral Unmixing," *IEEE Signal Process. Mag.* **19** (1), 2002, pp. 44–57.
24. http://www.cbrsp.org/cbrsp_toc_mb_chl_page.htm
25. <http://oceancolor.gsfc.nasa.gov/cgi/level3.pl>



MICHAEL K. GRIFFIN
is a staff member in the Sensor Technology and System Applications group. His current research focuses on applications of hyperspectral technology to meteorological and environmental applications. A recent effort involved the design and employment of a cloud-cover detection algorithm for the Hyperion hyperspectral sensor to run onboard the Earth Observing 1 (EO-1) space-based platform. He came to Lincoln Laboratory in 1997 to work on data analysis, algorithm development, and assessment of hyperspectral sensors. Prior to joining Lincoln Laboratory he was an atmospheric physicist at the Air Force Research Laboratory, where he was involved in the development of cloud algorithms from multispectral imagery and worked on the retrieval of humidity, precipitation, and surface properties from microwave sensor measurements. He received a B.S. degree in physics and mathematics from California State University, Chico, and M.S. and Ph.D. degrees in meteorology from the University of Utah.



HSIAO-HUA K. BURKE
leads the Sensor Technology and System Applications group at Lincoln Laboratory. In the area of remote sensing, she specializes in applications of optical sensors, particularly data analysis and algorithm development. A recent area of interest is the application of hyperspectral technology to Department of Defense needs, including fusion of hyperspectral data information with other sensors. She received her Ph.D. degree in atmospheric physics from Rice University, and joined Lincoln Laboratory as a staff member in 1981.



SU MAY HSU
is a staff member in the Sensor Technology and System Applications group. She researches hyperspectral image data analysis, focusing on background classification, target detection, and sensor fusion applications. Before joining Lincoln Laboratory in 1981, Su May worked in image data analysis for the General Electric Company in Schenectady, New York. She holds a B.S. degree from the National Taiwan University and a Ph.D. degree from Purdue University, both in electrical engineering.



SETH M. ORLOFF
is a staff member in the Sensor Technology and System Applications group. His concentrations include hyperspectral imagery, geographic information systems, multisensor fusion, image coregistration and geometric correction, and change detection. He received a B.A. degree in physics from Rice University, an M.A. degree in physics from the University of Texas in Austin, and a Ph.D. in space physics and astronomy from Rice University.



CAROLYN A. UPHAM
is an assistant staff member in the Sensor Technology and System Applications group. Her current research includes analysis of multispectral and hyperspectral data for atmospheric and background characterization, as well as modeling of chemical plumes. She received a B.S. degree in physics and meteorology and an M.S. degree in atmospheric science from the University of Massachusetts at Lowell.